Climbing film, flooding and falling film behavior in upflow condensation in tubes

CrossMark

Ilchung Park, Issam Mudawar *

Purdue University Boiling and Two-Phase Flow Laboratory (PU-BTPFL), Mechanical Engineering Building, 585 Purdue Mall, West Lafayette, IN 47907-2088, USA

ABSTRACT

Upflow condensation in vertical tubes is complicated by the relative magnitude of the opposing vapor shear and gravity. This study examines the different flow regimes for condensation of FC-72 in a vertical tube using both high-speed video imaging and detailed heat transfer measurements. Four regimes are identified, falling film, where the condensing film drains downwards by gravity opposite to low velocity vapor flow, oscillating film, corresponding to film flow oscillating between upwards and downwards, flooding, where film begins to be sheared upwards by the vapor core, and climbing film, where high vapor velocity causes the film to be sheared upwards. The four flow regimes are well segregated in a flow regime map based on dimensionless superficial velocities of the vapor and liquid. The condensation heat transfer coefficient is shown to decrease axially because of gradual thickening of the film, except for high mass velocities, where turbulence and intensified interfacial waviness cause downstream heat transfer enhancement. An annular flow model is constructed, which shows fair predictions for the climbing film regime. The predictive accuracy of the model is influenced by flow oscillations occurring downstream of the climbing film region and inability of the model to account for interfacial waves.

© 2013 Elsevier Ltd. All rights reserved.

1. Introduction

The recent increase in heat dissipation in electronic and power devices and systems has spurred interest in the development of compact, high-power-density phase-change thermal management systems that tackle both the heat acquisition from the device by boiling or evaporation, and the heat rejection to the ambient by condensation. These systems are becoming increasingly important to the development of high performance computers, electric vehicle power electronics, avionics, and directed energy laser and microwave weapon systems [1]. Different configurations have been proposed for heat acquisition by boiling, including pool boiling [2,3], channel flow boiling [4,5], jet [6–8] and spray [9,10], as well as enhanced surfaces [11,12] and hybrid cooling configurations [13,14]. However, far less emphasis has been placed on the condensation, or heat rejection part of these systems.

Much of the condensation knowhow and design models come from early research related to condensers found in power generation, chemical, and refrigeration and air conditioning industries. These condensers come in a variety of configurations, including falling film condensation on the outside of horizontal tubes in shell-and-tube heat exchangers, and inside horizontal, vertical and inclined tubes. The present study concerns internal upflow condensation in vertical tubes.

Condensation inside tubes takes the form of a number of flow regimes, which, in the order of decreasing quality, include pure vapor, annular, slug, bubbly and pure liquid [15]. Drastic differences in flow structure between these regimes have led investigators to construct flow regime maps and develop flow regime transition relations [16–21] that enable identification of regimes based on measurable parameters, and to develop models that are specific to individuals regimes. The annular regime, which consists of a thin film surrounding a vapor core, has been the focus of most studies on condensation in tubes because of its prevalence over a large fraction of the tube length and its ability to deliver very large heat transfer coefficients.

Vertical upflow condensation is encountered when the vapor is supplied upwards from the bottom of a vertical tube. At low vapor velocities, a *falling film* regime is encountered, where the condensing liquid film is driven downwards by gravity, opposite to the direction of the vapor flow. This regime is highly complicated by the role of interfacial waves, and is reminiscent of the complex interfacial behavior encountered in flow boiling at low velocities in vertical downflow [22–25]. Increasing the vapor velocity increases the vapor shear exerted on the film interface, which begins to slow the downward motion of the liquid film. A particular vapor velocity is reached that causes the interfacial portion of the film to be carried upwards rather than drain to the bottom. This condition

* Corresponding author. Tel.: +1 765 494 5705; fax: +1 765 494 0539.
E-mail address: mudawar@ecn.purdue.edu (I. Mudawar).
URL: https://engineering.purdue.edu/BTPFL (I. Mudawar).

Nomenclature

A	area
A^+	constant in eddy diffusivity function
$A_{f,*}$	flow area in liquid control volume
C	flooding constant
c_p	specific heat at constant pressure
D	diameter
f_i	interfacial friction factor
G	mass velocity
g	gravitational acceleration
h	condensation heat transfer coefficient
$\bar{h}$	condensation heat transfer coefficient averaged over region where $x < 1$
h_{fg}	latent heat of vaporization
j	superficial velocity
j^*	dimensionless superficial velocity
K	Von-Karman constant
k	thermal conductivity
$\dot{m}_f$	mass flow rate of FC-72 liquid film
$\dot{m}_{FC}$	total mass flow rate of FC-72
$\dot{m}_g$	mass flow rate of FC-72 vapor core
$\dot{m}_w$	mass flow rate of cooling water
P	pressure
P_f	perimeter
Pr	Prandtl number
Pr_T	turbulent Prandtl number
q	heat transfer rate
q''	heat flux at distance y from inner wall of inner stainless steel tube
q''_w	heat flux at inner wall of inner stainless steel tube
q_w	heat transfer rate from FC-72 to cooling water
Re_f	FC-72 film Reynolds number, $Re_f = G(1 - x)D_h/\mu_f$
T	temperature
t	time
T^+	dimensionless temperature
u	velocity
u^+	dimensionless liquid film velocity
u^*	friction velocity
u_f	local liquid film velocity
$\bar{u}_g$	mean vapor core velocity
x	mass quality
x_e	thermodynamic equilibrium quality
y	distance perpendicular to inner wall of inner stainless steel tube
y^+	dimensionless distance perpendicular to inner wall of inner stainless steel tube
z	stream-wise distance

Greek Symbols

Γ_{fg}	rate of mass transfer due to condensation per unit distance
δ	thickness of condensing film
δ^+	dimensionless film thickness
ε_m	eddy momentum diffusivity
ε_h	eddy heat diffusivity
μ	dynamic viscosity
v	kinematic viscosity
ρ	density
σ	surface tension
τ	shear stress

Subscripts

c	vapor core
exp	experimental, measured
f	saturated liquid; liquid film
FC	FC-72
g	saturated vapor; vapor core
i	interfacial; inner wall of inner stainless steel tube
in	inlet
o	outer wall of inner stainless steel tube
out	outlet
$pred$	predicted
sat	saturation
ss	inner stainless steel tube
w	water; wall
$wall$	wall of inner stainless steel tube

is termed the *onset of flooding*, or simply the *flooding* point [26]. There is a finite vapor velocity range between the onset of flooding and the condition where the entire liquid film begins to be carried upwards. Above the latter condition, *climbing film* flow is achieved, as the vapor shear begins to dwarf the influence of gravity.

The ability to predict flooding is crucial to the design and operation of condensers in which vapor flows upward. However, a survey of the flooding literature by Bankoff and Lee [26] (i) points to most findings being based on experiments performed in relatively large diameter tubes, and (ii) reveals a dearth of reliable predictive tools. The most popular predictive tool for flooding is a relation by Wallis [27] that is based on the densities and superficial velocities of the vapor and liquid, and the tube diameter. Various attempts were made to improve the Wallis relation by incorporating the influences of additional parameters such as inlet and exit geometries, inclination angle, and other fluid properties [28–37]. However, the complexity of the flooding mechanism has led some to the conclusion that no reliable correlations or models are available that can accurately predict the onset of flooding with reasonable accuracy for different geometries and fluid types [38]. In general, the vapor velocity corresponding to the onset of flooding increases with increasing tube diameter [36,39], decreasing liquid viscosity [29] and increasing surface tension [35,40]. Attempts have been

made to ascertain the effects of tube inclination for tubes with small diameters [41] and larger ones [42,43]. It is recommended that the use of empirical correlations for flooding be limited to the ranges of flow rates, fluid properties, and tube geometries of the databases these correlations are based upon [33].

A few theoretical models have been based on the notion that flooding is related to the interaction of vapor flow with a wavy liquid film interface. Several attempts were made to model the flooding mechanism theoretically by exploring wave growth using stability analysis [44–48]. Other models are based on vapor shear as the primary means for momentum transfer [49–51]. A few studies involved the use of commercial computational fluid dynamics (CFD) codes [52] to estimate the forces acting on a standing wave just before flooding is initiated.

The concurrent motion of the vapor and liquid film renders *climbing film* flow more easily predictable using popular models and correlations for annular flow condensation, especially where the effects of gravity are negligible compared to those of vapor shear.

The primary objective of the present study is to explore the various flow regimes that are encountered in upflow condensation of FC-72 in tubes. High-speed video imaging is used to investigate the interfacial interactions within each regime, and to construct a

corresponding flow regime map. Next, detailed heat transfer measurements are used to explore differences in the transport behavior among the different condensation regimes, subject to variations in the mass velocities of the FC-72 and cooling water. A control volume based model is then constructed to predict heat transfer in the *climbing film* regime. Long term, the findings from this study will be used to ascertain the influence of body force on flow condensation in tubes by comparing data for condensation in horizontal flow, upflow and downflow [53] with those in microgravity [54]. This comparison will help identify the minimum mass velocity (*i.e.,* minimum pumping power) that would negate the influence of body force on flow condensation in space vehicles.

2. Experimental methods

2.1. Condensation flow loop

The condensation facility constructed for the present study is comprised of three flow loops: a primary loop for the condensing fluid, FC-72, and two water cooling loops. As shown in Fig. 1(a), heat is transferred from the primary loop to the first water loop

via the condensation test module, and to the second water cooling loop via a separate condenser. Fig. 1(b) shows a photo of the entire facility.

FC-72 is a clear, colorless and odorless perfluorinated fluid made by 3M-company. It has a boiling point of 56 °C at atmospheric pressure, and its latent heat and surface tension are one order of magnitude smaller than those for water. Table 1 provides representative thermophysical properties of FC-72 at 58 °C, which is the saturation temperature corresponding the average operating pressure (1.071 bar) for the present study.

In the primary loop, most of the FC-72 liquid is contained in a sealed reservoir, from which the liquid is circulated through the loop with the aid of a gear pump. The liquid flows through one of several rotameters connected in parallel, following which it is converted to vapor by a 14.2 kW Watlow Cast-X 3000 pre-heater. The pre-heater's PID temperature controller is set to ensure slightly superheated vapor conditions at the pre-heater's outlet. The FC-72 vapor is then supplied to the condensation module, inside which it is converted to liquid by rejecting heat to a counter-flow of water from the first water loop. The two-phase FC-72 mixture is then cooled through a plate-type condenser by rejecting heat to the
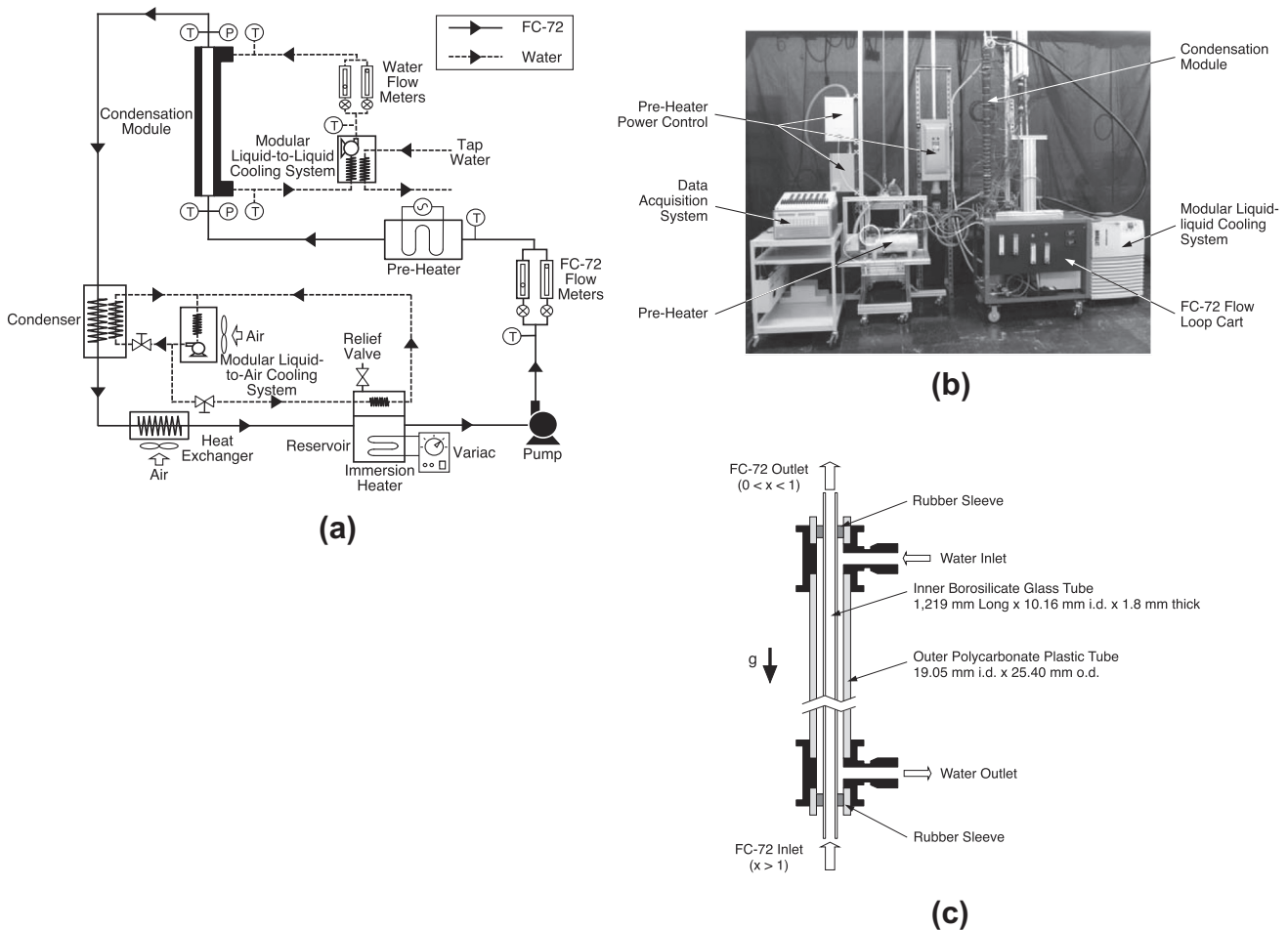
Fig. 1. (a) Schematic diagram of condensation facility. (b) Photo of facility. (c) Construction of condensation module for flow visualization studies.

Table 1
Thermophysical properties of saturated FC-72 at 58 °C (*P* = 1.071 bar).

k_f (W/m K)	μ_f (kg/m s)	$c_{p,f}$ (J/kg K)	σ (mN/m)	h_{fg} (kJ/kg)	ρ_f (kg/m³)	ρ_g (kg/m³)
0.0536	427×10^{-6}	1104	8.21	94.36	1589	14.00

Water

Compression
Fitting

O-ring

Outer Tubing

Brass
Adaptors

FC-72

Inner Tube

Screws

T-type Thermocouples
In SS Sheathing

SS 304 Inner Tube
11.89 mm i.d. x 0.41 mm Thick

SS 304 Outer Tube
22.48 mm i.d. x 3.05 mm Thick

(a)

FC-72 Outlet
(0 < x < 1)

Water
Inlet

139.7 mm

1259.84
mm

139.7 mm

76.2 mm

76.2 mm

38.1 mm

38.1 mm

Water
Outlet

FC-72 Inlet
(x > 1)

(b)
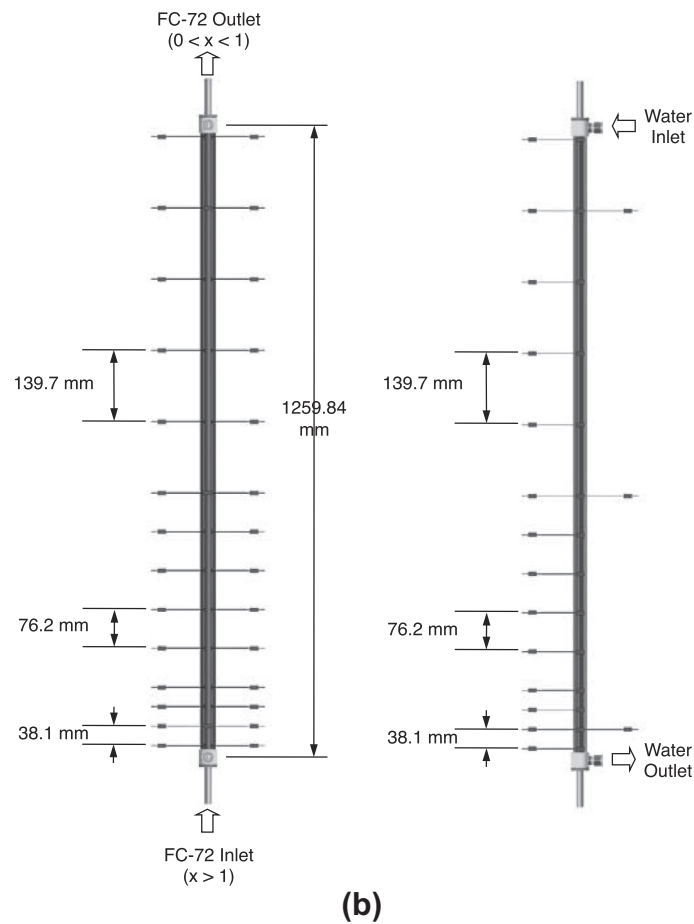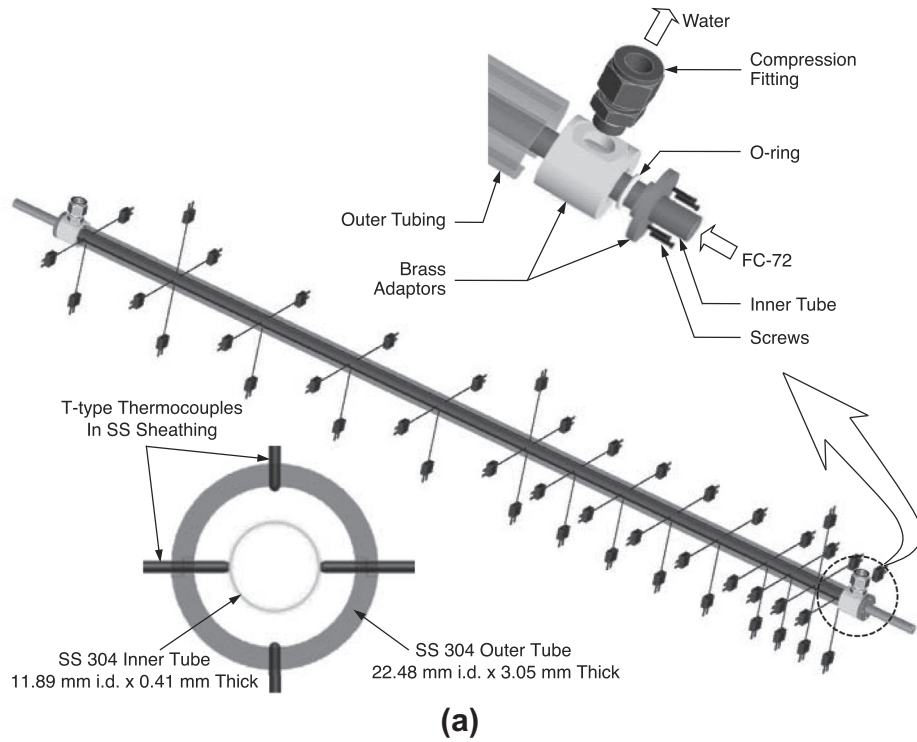
Fig. 2. (a) Construction of condensation module for heat transfer measurements. (b) Location of thermocouples for temperature measurements of outer wall of inner tube and cooling water.

second water cooling loop. An air-cooled condenser situated downstream from the plate condenser is used to condense any residual vapor and convert the FC-72 to sub-cooled liquid as it returns to the reservoir.

The FC-72 temperature and pressure are measured at several locations in the primary loop. The temperature is measured at the pre-heater's inlet, and the temperature and pressure at both the inlet and outlet of the condensation module.

The first water cooling loop is comprised of a 14-kW modular Lytron LCS cooling system and several rotameters. This system contains a reservoir, pump and liquid-to-liquid heat exchanger; the latter is used to reject the heat absorbed from the FC-72 to tap water. The water temperature is measured at the inlet and outlet of the condensation module. The second water cooling loop consists of a 1.46-kW modular Lytron cooling system containing a reservoir, pump and water-to-air heat exchanger; the latter is used to reject heat from the FC-72 to ambient air.

Deaeration of the FC-72 is achieved in the primary loop's reservoir using two 300-W immersion heaters and a condensation coil that is cooled by a bypass from the second water cooling loop. The deaeration is achieved by vigorously boiling the FC-72 liquid and condensing the FC-72 vapor for 30 min, while allowing non-condensable gases to escape to the ambient.

2.2. Condensation module for flow visualization

Two separate condensation modules are used in this study, one for flow visualization and the other for heat transfer measurements. The two condensation modules have fairly similar dimensions, but are constructed from different materials.

Fig. 1(c) shows the transparent tube-in-tube construction of the condensation module for flow visualization. The FC-72 flows upwards through the inner tube, and the water downwards through the annulus between the inner and outer tubes. The inner tube is made from borosilicate glass and has a 10.16-mm i.d., wall thickness of 1.8 mm and length of 1219 mm. The outer tube is made from polycarbonate plastic (Lexan), which, like the inner tube, features high transparency but possesses a much lower thermal conductivity. The outer tube has a 19.05-mm i.d. and 25.4-mm o.d. Short latex rubber sleeves are inserted between the inner the outer tubes, leaving a condensation length of 1143 mm for flow visualization. The inlet and outlet of the flow visualization module are fitted with Type-T thermocouples and pressure transducers. Both the inlet and outlet of the waterside are fitted with type-T thermocouples.

Flow visualization is achieved with the aid of a high-speed Photron Fastcam Ultima APX video camera system capable of shutter speeds up to 1/120,000 s, which is fitted with a Nikon 105-mm F/2.8D magnification lens. The camera is mounted normal to the front of the condensation module, with high intensity back lighting provided by an array of 15 high power white 5-W LEDs. Flow visualization is performed in inlet, middle and outlet 381-mm long regions centered at 190, 571, and 952 mm, respectively, from the inlet.

2.3. Condensation module for heat transfer measurements

The overall design of the condensation module intended for heat transfer measurements is similar to that of the flow visualization module except for the use of different materials to facilitate accurate heat transfer measurements. Fig. 2(a) shows both the inner and outer tubes of the condensation module for heat transfer measurements are made from 304 stainless steel. The inner tube has an 11.89-mm i.d. and wall thickness of 0.41 mm, and the outer tube 22.48-mm i.d. and 3.05-mm wall thickness. The total condensation length of this module is 1259.8 mm. Two main goals with the construction of this module are to minimize resistance to radial heat conduction between the FC-72 and water, and minimize axial wall conduction effects. A compromise between these goals is achieved by a combination of the small thickness of the inner tube and relatively low thermal conductivity of the stainless steel wall. The outer tube is wrapped with a thick layer of fiberglass insulation to minimize heat loss to the ambient.

This module contains the same types of temperature and pressure instrumentation at the inlets and outlets for both fluids as the flow visualization module. However, the condensation module for heat transfer measurements features an additional 45 type-T thermocouples, 28 of which are attached to the outer surface of the inner tube in 14 diametrically opposite pairs as illustrated in Fig. 2(b). Notice that the axial distance between thermocouples is smallest, 38.1 mm, in the FC-72 inlet region, and increases axially to 76.2 mm in the middle, and 139.7 mm near the outlet. This distribution is intended to capture the large variations in wall temperature near the inlet with high resolution.

For the waterside, 14 thermocouples are inserted into the annulus at the same axial locations as the wall thermocouples. There are also three thermocouples mounted diametrically opposite to three of the 14 main water thermocouples, which are intended to capture any asymmetry in the water temperatures. All thermocouples are made from 0.21-mm diameter thermocouple wire with a bead diameter of 0.79 mm.

2.4. Operating conditions and measurement uncertainty

Two series of experiments are performed using the two condensation modules. The first, which is performed using the flow visualization module, is focused on capturing the detailed interfacial behavior of the condensing film at the three aforementioned axial locations. The second series of tests is dedicated to heat transfer measurements using the second condensation module. In both

Table 2
Experimental operating conditions for the flow visualization study.

	FC-72					Cooling water			q_w (W)	$x_{e,out}$	$Re_{f,out}$
	$x_{e,in}$	$\dot{m}_{FC}$ (g/s)	G_{FC} (kg/m² s)	$T_{FC,in}$ (°C)	$P_{FC,in}$ (kPa)	$\dot{m}_w$ (g/s)	G_w (kg/m² s)	ΔT_w (°C)			
Max.	1.14	12.93	159.49	72.93	114.01	133.29	977.79	23.29	702.48	0.70	1751.9
Min.	1.00	1.08	13.32	57.41	102.00	0.83	6.09	1.14	80.85	0.00	239.5

Table 3
Experimental operating conditions for the condensation heat transfer data.

	FC-72					Cooling water			q_w (W)	$x_{e,out}$	$Re_{f,out}$
	$x_{e,in}$	$\dot{m}_{FC}$(g/s)	G_{FC} (kg/m² s)	$T_{FC,in}$ (°C)	$P_{FC,in}$ (kPa)	$\dot{m}_w$(g/s)	G_w (kg/m² s)	ΔT_w (°C)			
Max.	1.16	42.99	387.04	74.86	152.62	84.97	314.48	20.56	2240.4	0.70	4548.3
Min.	1.01	1.08	9.73	54.95	93.83	0.83	3.08	6.01	43.7	0.00	101.3

Falling Film

Gravity ⬇

⬆ Flow

(a)

Flooding

(b)

Climbing Film

(c)

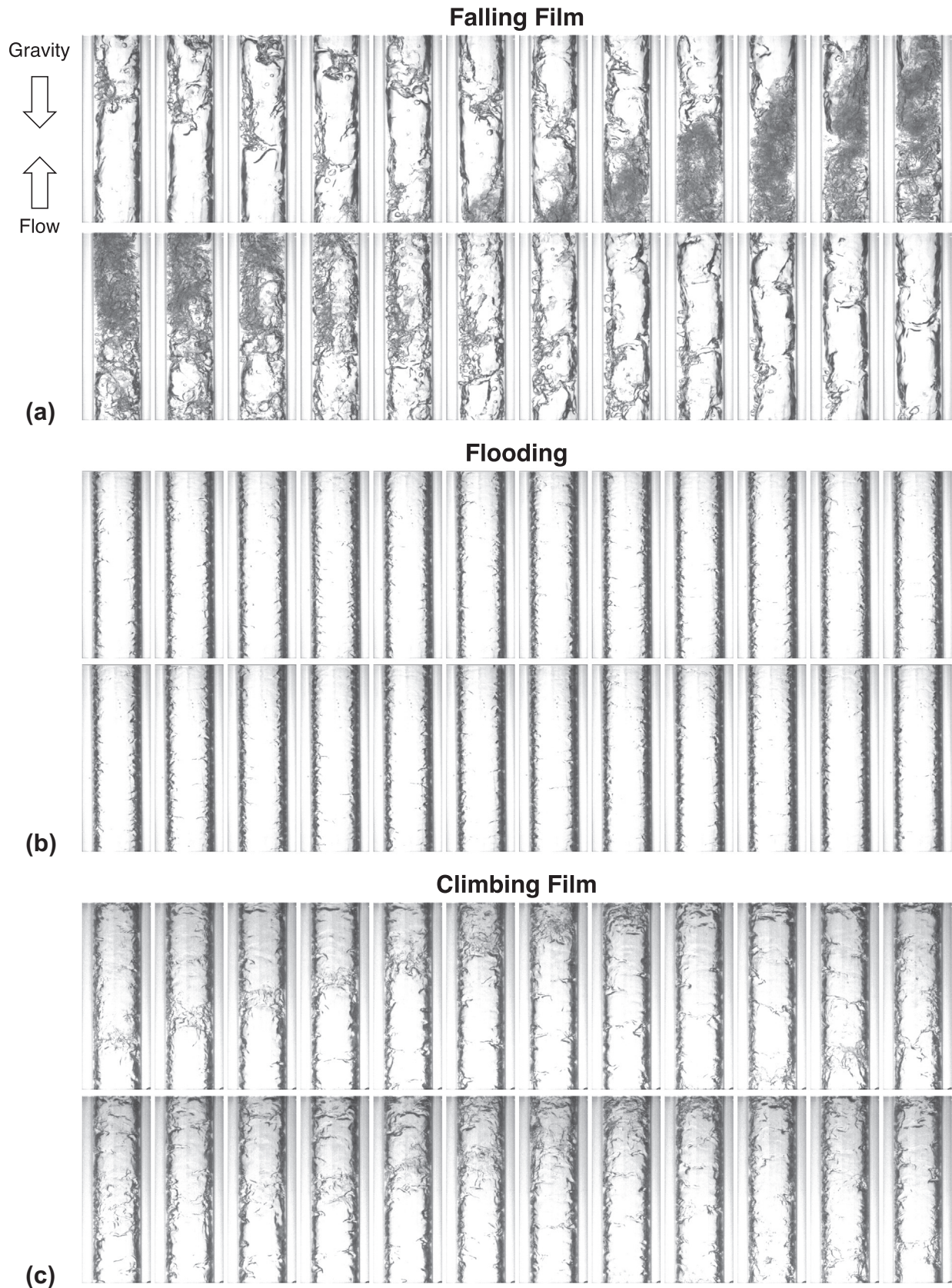**Fig. 3.** Sequential images of (a) *falling film* in inlet region (centered at z = 190 mm) with G_{FC} = 13.32 kg/m^2 s and G_w = 6.09 kg/m^2 s, (b) flooding in inlet region with G_{FC} = 53.29 kg/m^2 s and G_w = 73.36 kg/m^2 s, and (c) climbing film in outer region (centered at z = 952 mm) with G_{FC} = 106.45 kg/m^2 s and G_w = 97.79 kg/m^2 s. Individual images in each sequence are separated by 0.0125 s.

series of tests, the thermodynamic equilibrium quality of FC-72 at the inlet is maintained slightly above unity to achieve annular flow over the entire condensation length.

The flow visualization experiments consist of 65 sets of operating conditions. As indicated in Table 2, these include nine different FC-72 mass velocities in the range of G_{FC} = 13.32–159.49 kg/m^2 s and a broad range of water mass velocities of G_w = 6.09–977.79 kg/m^2 s. Table 2 provides the values of FC-72 inlet quality, $x_{e,in}$, inlet temperature, $T_{FC,in}$, and inlet pressure, $P_{FC,in}$. Also indicated are the amount of heat transferred from FC-72 to cooling water, q_w, and the outlet thermodynamic equilibrium quality of FC-72, $x_{e,out}$, and outlet FC-72 film Reynolds numbers, $Re_{f,out}$.

The test matrix for the heat transfer measurements consists of 69 sets of operating conditions. As indicated in Table 3, these tests include 14 FC-72 mass velocities in the range of G_{FC} = 9.73–387.04 kg/m^2 s and 5 water mass velocities for each FC-72 mass velocity. To preclude uncertainties that may arise from cooling water entrance effects, heat transfer data are measured only within the upstream condensation length of z = 0–807.7 mm. The inlet quality of FC-72 is maintained in the range of $x_{e,in}$ = 1.01–1.16, which results in an upstream single-phase superheated vapor region 1.62–193.8-mm long (0.2–24.0% of the 807.7 mm length considered in the heat transfer measurements). The inlet temperature and pressure of FC-72 are $T_{FC,in}$ = 54.95–74.86 °C and $P_{FC,in}$ = 93.83–152.62 kPa, respectively, and the amount of heat transferred between the two fluids is 43.7 to 2240.4 W. These operating conditions result in FC-72 outlet thermodynamic equilibrium qualities and outlet film Reynolds numbers of $x_{e,out}$ = 0–0.70 and $Re_{f,out}$ = 101.3–4548.3, respectively.

The pressure transducers used throughout the condensation facility possess a measurement uncertainty of ±0.5%. The uncertainties of the thermocouples are smaller than ±0.4 °C. Uncertainties in the outer diameter and wall thickness of the condensing tube used for heat transfer measurements are ±0.08 mm and ±0.03 mm, respectively. The uncertainties of the outer diameter and wall thickness of the outer tube of the same condensation module are ±0.13 mm and ±0.18 mm, respectively. Combining these uncertainties with the uncertainties in determining fluid properties yields overall uncertainties in determining heat transfer rate, vapor quality, and condensation heat transfer coefficient of ±7.11%, ±6.52%, and ±7.60%, respectively.

3. Flow visualization results

3.1. Condensation regimes

Before discussing the results of the flow visualization condensation module, it is important to point out that, because the FC-72 film covers the entire inner wall of the inner tube, the captured video images represent two separate interfaces overlaid on one another. This renders any detailed measurements of the film's interface very illusive. Despite this limitation, the module construction and optical methods used provide clear and interpretable differences in interfacial behavior for different operating conditions.

Fig. 3(a)–(c) show sequential images of the FC-72 condensation film along the inner wall of the glass tube for three representative flow conditions: falling film, flooding, and climbing film. The total duration of each sequence is 0.3 s, with individual images in each sequence separated by 0.0125 s. The flow conditions are segregated by the popular Wallis relation [27] for flooding in tubes

$$\sqrt{j_g^*} + \sqrt{j_f^*} = C, \qquad (1)$$

where C is a constant whose magnitude generally depends on the tube geometry and fluid properties, and j_g^* and j_f^* are dimensionless superficial velocities of vapor and liquid, respectively, which are defined as
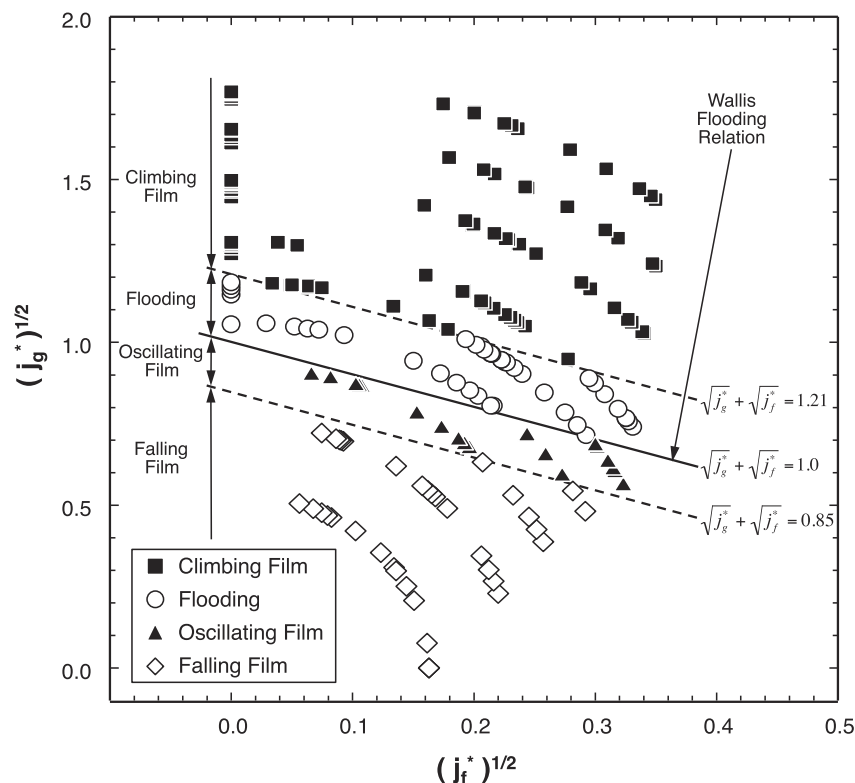
Fig. 4. Flow regime map for condensation of FC-72 in flow visualization module with D_i = 10.16 mm.

$$j_g^* = \frac{j_g}{\sqrt{gD_i(\rho_f - \rho_g)/\rho_g}} \qquad (2a)$$

and

$$j_f^* = \frac{j_f}{\sqrt{gD_i(\rho_f - \rho_g)/\rho_f}} . \qquad (2b)$$

It should be noted that the temperatures of both the FC-72 and cooling water are assumed to vary linearly along the condensation length when computing the superficial velocities from the experimental data.

Fig. 3(a) shows images of the liquid film captured in the inlet region, centered at $z = 190$ mm, where the liquid film is moving downwards while the vapor moves upwards. This *falling film* behavior occurs when the vapor velocity is low and the influence of gravity on liquid motion is very significant. The superficial velocities of liquid and vapor for the flow condition in Fig. 3(a) are $j_f = 0.0010$ m/s and $j_g = 0.87$ m/s, respectively. Notice that the falling liquid film's interface for a portion of the inlet region is momentarily laminar with an appearance of annular flow. Because of the unstable interface, wave peaks from opposite sides of the tube quickly merge, capturing some vapor bubbles in the film, which also causes breakup of liquid into ligaments and droplets. Some of the shattered liquid is entrained upwards with the vapor flow, the rest appears to redeposit on the liquid film. The chaotic combination of falling film, upward moving vapor core, entrained vapor bubbles, and shattered liquid momentarily produces a highly mixed two-phase mixture, which is quickly replaced by the initial laminar film, and the process is repeated in a cyclical fashion.
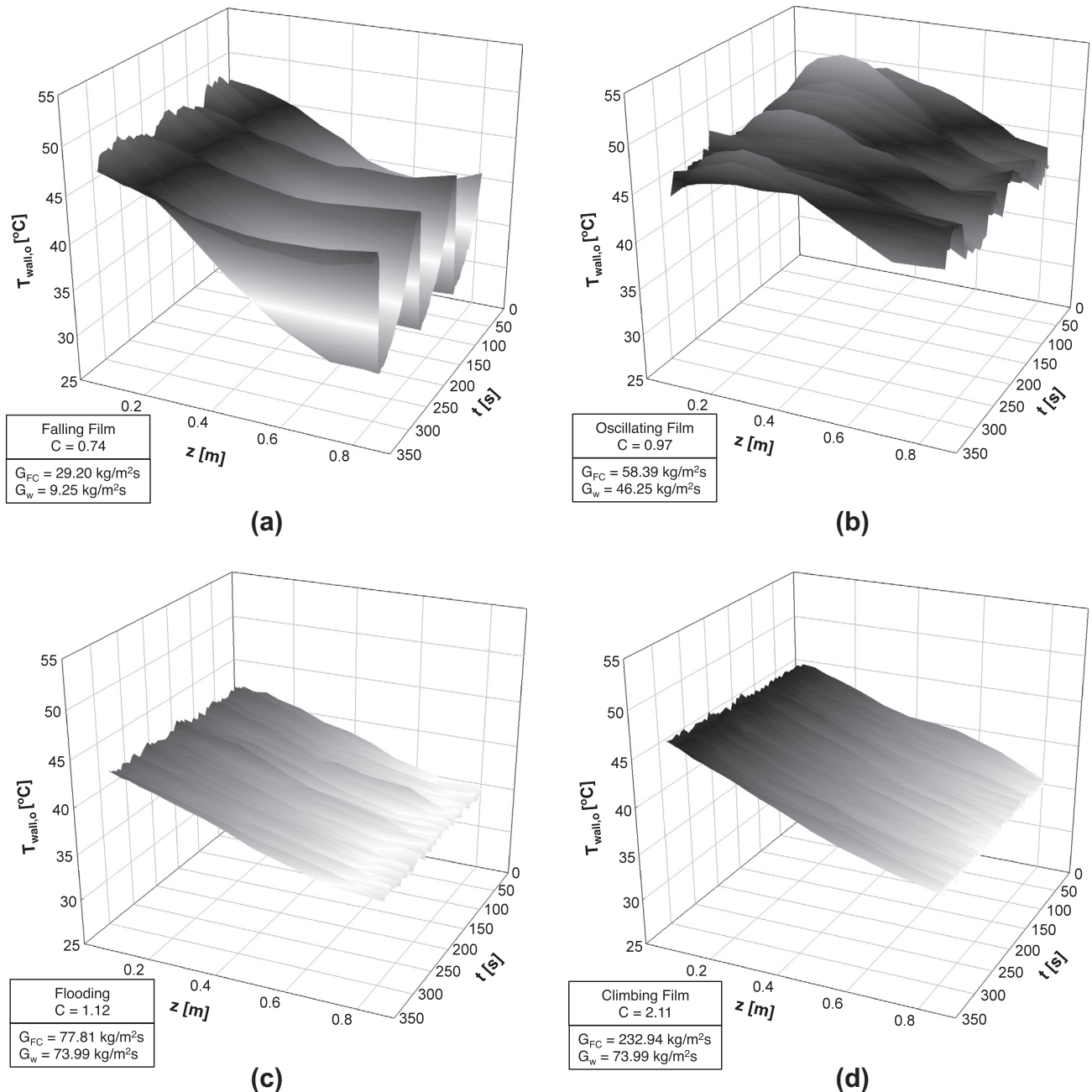
Fig. 5. Variation of temporal record of outside tube wall temperature, $T_{wall,o}$, along condensation length for (a) $G_{FC} = 29.20$ kg/m² s and $G_w = 9.25$ kg/m² s, (b) $G_{FC} = 58.39$ kg/m² s and $G_w = 46.25$ kg/m² s, (c) $G_{FC} = 77.81$ kg/m² s and $G_w = 73.99$ kg/m² s, and (d) $G_{FC} = 232.94$ kg/m² s and $G_w = 73.99$ kg/m² s.
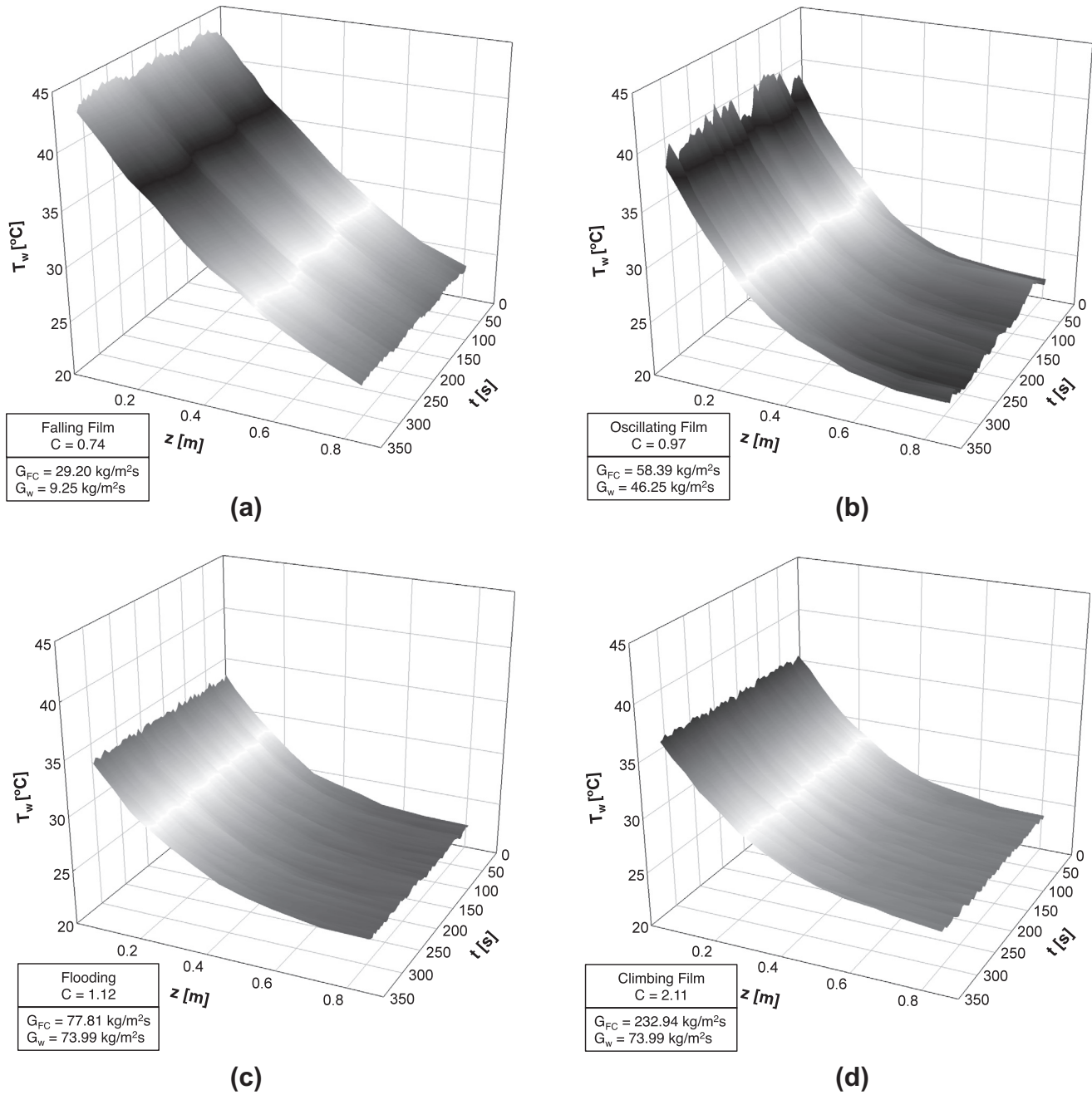
Fig. 6. Variation of temporal record of water temperature, T_w, along condensation length for (a) G_{FC} = 29.20 kg/m² s and G_w = 9.25 kg/m² s, (b) G_{FC} = 58.39 kg/m² s and G_w = 46.25 kg/m² s, (c) G_{FC} = 77.81 kg/m² s and G_w = 73.99 kg/m² s, and (d) G_{FC} = 232.94 kg/m² s and G_w = 73.99 kg/m² s.

Notice that the motion of the annular liquid film is governed by the relative magnitude of the upward shear stress exerted by the vapor core and the downward gravity. The behavior captured in Fig. 3(a) is representative of relatively weak vapor shear. As the vapor velocity is increased, a condition is achieved where the shear force begins to balance the body force, which results in a fairly stagnant liquid at the film's interface. *Flooding*, which is predicted according to the Wallis relation [27], is a condition that refers to flow behavior associated with this force equilibrium since a further increase in the vapor velocity will cause the liquid film to commence climbing upwards.

Fig. 3(b) captures interfacial behavior in the inlet region, centered at z = 190 mm, corresponding to the onset of *flooding*

resulting from a vapor superficial velocity of j_g = 3.64 m/s, much higher than that for Fig. 3(a), and a lower superficial liquid velocity of j_f = 0.009 m/s. Notice that the motion of the liquid film is barely noticeable at the onset flooding. The interface of the liquid film is marred by a combination of small ripples and large waves, which appear to be induced by the high vapor shear.

As the superficial velocities of liquid and vapor are increased appreciably, the liquid film flow is firmly upwards. This *climbing film* flow is depicted in Fig. 3(c) for the outer region, centered at z = 952 mm, corresponding to j_g = 5.50 m/s and j_f = 0.0198 m/s. Here, the liquid film is shear-driven upwards, with the interface marred by both ripples and relatively large waves that are induced by the high vapor shear.
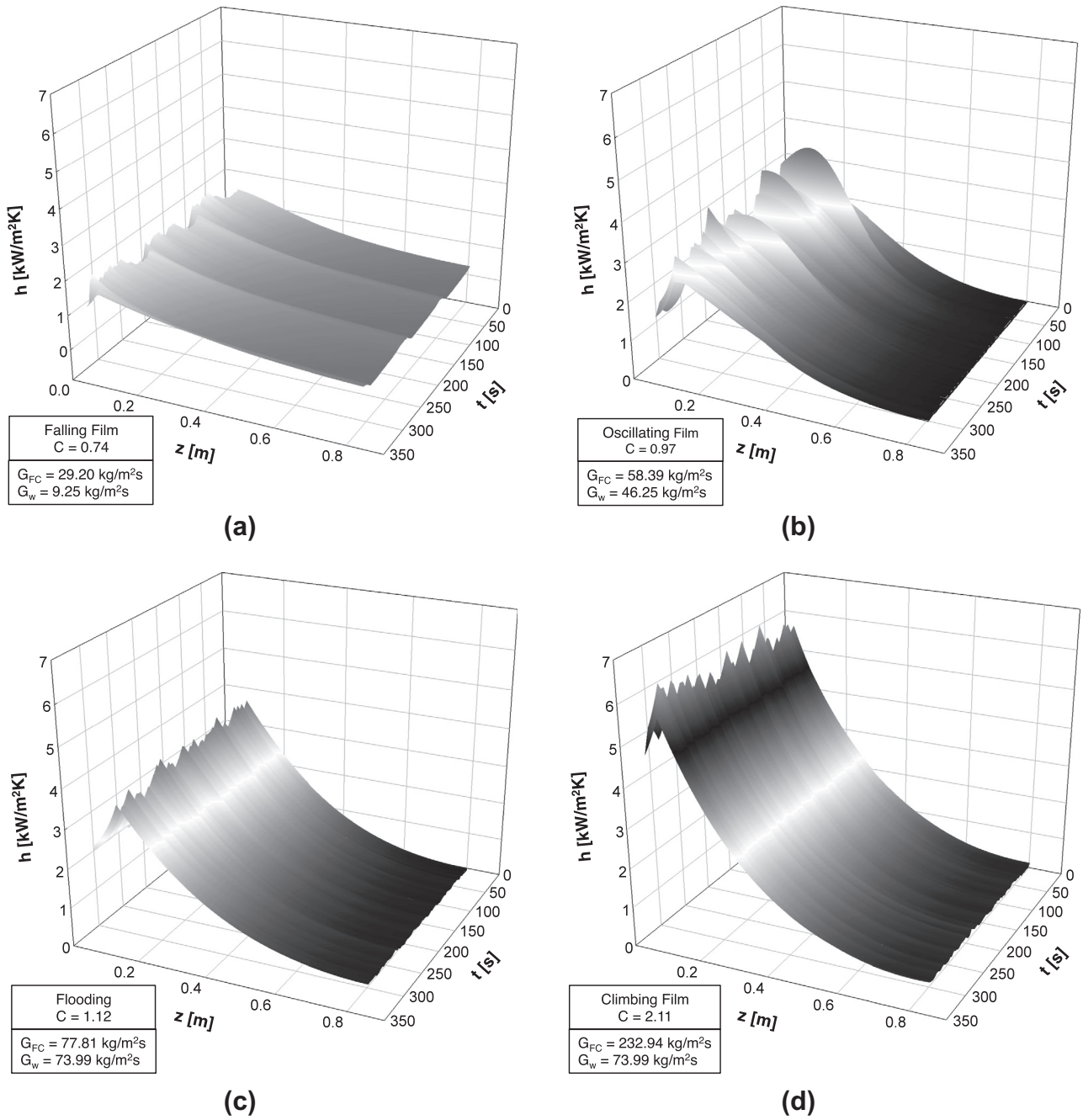
Fig. 7. Variation of temporal record of local condensation heat transfer coefficient, *h*, along condensation length for (a) G_{FC} = 29.20 kg/m² s and G_w = 9.25 kg/m² s, (b) G_{FC} = 58.39 kg/m² s and G_w = 46.25 kg/m² s, (c) G_{FC} = 77.81 kg/m² s and G_w = 73.99 kg/m² s, and (d) G_{FC} = 232.94 kg/m² s and G_w = 73.99 kg/m² s.

3.2. Flow regime map

After careful examination of video records for different operating conditions, flow behavior appears to fall into one of four distinct regimes: *falling film*, *oscillating film*, *flooding*, and *climbing film*. The *oscillating film* regime can be described as follows. The liquid film incurs flooding for a short duration, but, as more condensate accumulates in the film, the film gets thicker and begins to exhibit falling film behavior. The liquid film appears quite thin for a short period, allowing the downward body force to be balanced by the upward vapor shear, and the film *incurs flooding*. But, with the condensation increasing liquid mass, the film becomes thicker, and the downward body force begins to exceed

the vapor shear, causing the flow to switch to that of a falling film. This in turn causes a thinning of the liquid film and temporary flooding followed by re-thickening and repeat of the falling film behavior in a sequential manner.

The four flow regimes are used to construct a flow regime map for upward condensing flows using coordinates based on the Wallis dimensionless superficial velocities defined in Eqs. 2(a) and 2(b). Fig. 4 shows the Wallis relation with *C* = 1 predicts data corresponding to the *onset of flooding* with good accuracy. *Falling film* flow is achieved when *C* < 0.85 (*C* = 0.56 for Fig. 3(a)), *oscillating flow* 0.85 < *C* < 1.0, *flooding* 1.01 < *C* < 1.21 (*C* = 1.10 for Fig. 3(b)), and *climbing film C* > 1.21 (*C* = 1.52 for Fig. 3(c)).

4. Heat transfer results

4.1. Heat transfer data reduction

A thermal model is constructed to determine the local condensation heat transfer coefficient in the condensation module intended for heat transfer measurements. As discussed in [53], the film interface is assumed to maintain saturation temperature, $T_{sat}(z)$, which is determined from the pressure measurements. Given the very small pressure drop across the condensation length, the saturation pressure, $P_{sat}(z)$, used to determine $T_{sat}(z)$ is calculated from a linear curve fit between the measured inlet pressure, P_{in}, and outlet pressure, P_{out}. The water temperature, $T_w(z)$, and outer wall temperature of the inner tube, $T_{wall,o}(z)$, are determined from curve fits to their respective measured values. A differential amount of heat, dq, which is equal to the differential rise in sensible energy of the cooling water, is transferred from the FC-72 to the cooling water. The thermal model for the region $x_e < 1$ is represented by the relation

$$dq = (\pi D_i dz) h (T_{sat} - T_{wall,i}) = \frac{T_{wall,i} - T_{wall,o}}{\frac{\ln(D_o/D_i)}{2\pi k_{ss} dz}} = \dot{m}_w c_{p,w} dT_w, \qquad (3)$$

which is used to determine the local condensation heat transfer coefficient, $h(z)$, of FC-72. For the small superheated inlet region before the liquid film begins to develop, the temperature of the superheated FC-72 vapor, $T_g(z)$, is determined from the energy balance

$\dot{m}_{FC} c_{p,g} dT_g = \dot{m}_w c_{p,w} dT_w$, and the thermodynamic equilibrium quality for the superheated region is given by

$$x_e = 1 + \frac{c_{p,g}(T_g - T_{sat})}{h_{fg}}. \qquad (4)$$

Eq. (4) is also used to determine the location where $x_e = 1$. The heat transfer coefficient for the superheated region is obtained by replacing T_{sat} in Eq. (3) with the local temperature of the superheated vapor.

$$dq = (\pi D_i dz) h (T_g - T_{wall,i}) = \frac{T_{wall,i} - T_{wall,o}}{\left[\frac{\ln(D_o/D_i)}{2\pi k_{ss} dz}\right]} = \dot{m}_w c_{p,w} dT_w. \qquad (5)$$

For the saturated region ($x_e < 1$), the local flow rate of the condensing film, $\dot{m}_f(z)$, is obtained by integrating the relation $d\dot{m}_f = dq/h_{fg}$ from the location where $x_e = 1$. The local thermodynamic equilibrium quality in the same region is given by $x_e = (\dot{m}_{FC} - \dot{m}_f)/\dot{m}_{FC}$.

4.2. Temporal and spatial records of heat transfer parameters

Figs. 5–7 show spatial records of outer condensation tube wall temperature, $T_{wall,o}$, water temperature, T_w, and condensation heat transfer coefficient, h, measured along the condensation length *after* reaching steady state conditions. Shown are results for four sets of operating conditions representative of *falling film*, *oscillating film*, *flooding* and *climbing film* regimes. Despite waiting until all system pressures and temperatures reach steady state before making these measurements, relatively high wall temperature
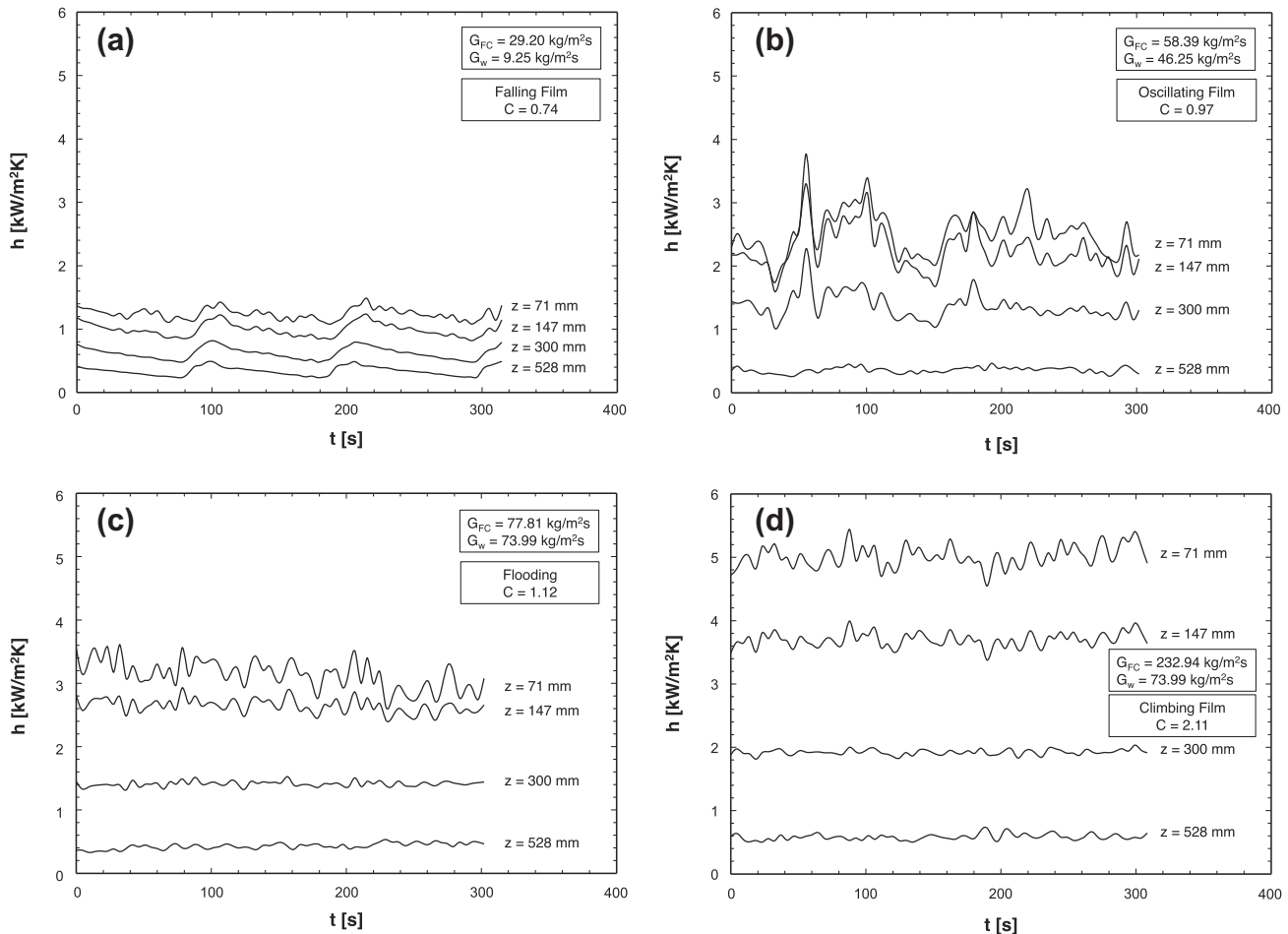
Fig. 8. Temporal records of condensation heat transfer coefficient at four axial locations for (a) $G_{FC} = 29.20$ kg/m^2 s and $G_w = 9.25$ kg/m^2 s, (b) $G_{FC} = 58.39$ kg/m^2 s and $G_w = 46.25$ kg/m^2 s, (c) $G_{FC} = 77.81$ kg/m^2 s and $G_w = 73.99$ kg/m^2 s, and (d) $G_{FC} = 232.94$ kg/m^2 s and $G_w = 73.99$ kg/m^2 s.

fluctuations are persistent in both the *falling film* and *oscillating film* regimes as shown in Figs. 5(a) and (b) respectively. These regimes correspond to low FC-72 mass velocities (G_{FC} = 29.20 kg/m² s for *falling film* and 58.39 kg/m² s for *oscillating film*) and relatively low values of parameter C in Eq. (1) (C = 0.74 for *falling film* and 0.97 for *oscillating film*), based on the flow regime map presented earlier. Notice that the temperature fluctuations are more pronounced but more periodic for the *falling film* regime, compared to a less pronounced but more chaotic response for the *oscillating film* regime. Additionally, the temperature fluctuations are more severe in the exit region compared to the inlet and middle regions for both regimes. The amplitude of temperature fluctuations is greatly diminished for the *flooding* and *climbing film* regimes as shown in Figs. 5(c) and (d), respectively. These regimes correspond to relatively high mass velocities (G_{FC} = 77.81 kg/m² s for *flooding* and 232.94 kg/m² s for *climbing film*), and relatively high C values of 1.12 and 2.11 for the *flooding* and *climbing film* regimes, respectively.

As shown in Fig. 6(a)–(d), the variations of water temperature, T_w, are similar in overall trend to those of the wall temperature. While the amplitude of water temperature fluctuations is much smaller than that for the wall temperature, the water temperature fluctuations are slightly more pronounced for the *falling film* and *oscillating film* than for the *flooding* and *climbing film* regimes.

Fig 7(a)–(c) show the variations of the local condensation heat transfer coefficient, h, derived from those for the wall and water temperatures. Here too, the variations follow the general trends displayed in Figs. 5(a)-(d) and 6(a)–(d).

Fig. 8(a)–(d) show temporal variations of the condensation heat transfer coefficient, h, at four different axial locations of z = 71, 147, 300 and 528 mm from the inlet of the condensation length. Notice that these variations are fairly periodic for the *falling film* regime,

Fig. 8(a), and both more severe and more chaotic for the *oscillating film* regime, Fig. 8(b). The percentage amplitude is greatly diminished both for the *flooding* regime, Fig. 8(c), and *climbing film* regime, Fig. 8(d). It should be noted that all temperature measurements are averaged over an adequate time period to obtain the heat transfer results discussed hereafter.

4.3. Heat transfer trends

Fig. 9(a) shows axial variations of the outer wall temperature of the inner tube, $T_{wall,o}$, and the cooling water temperature, $T_w(z)$, for four different combinations of FC-72 and water mass velocities. Both temperature distributions are determined from third-order polynomial curve fits to axial distance. These distributions are then used to calculate the corresponding variations depicted in Fig. 9(b) for the amount of heat transferred from the FC-72 to the cooling water per unit length, dq/dz, using Eqs. (3) and (5), and the FC-72 mass quality, x, using $x = (\dot{m}_{FC} - \dot{m}_f)/\dot{m}_{FC}$. Fig. 9(b) shows dq/dz for all FC-72 mass velocities is highest in the upstream region, where the condensate film is thinnest, and decreases gradually towards the outlet because of the increasing film thickness. Additionally, dq/dz increases with increasing mass velocity of FC-72 because of the increased vapor shear. As expected, Fig. 9(b) shows x is highest in the upstream region and decreases gradually towards the outlet. Notice that dq/dz subsides for all mass velocities to very low values at the outlet, where values of x below 0.68 indicate the annular liquid film can no longer be maintained.

Fig. 10(a)–(d) show the variations of the experimentally determined local FC-72 heat transfer coefficient, h, with axial distance in both the single-phase superheated vapor and film condensation regions for FC-72 mass velocities of G_{FC} = 29.20, 58.39, 194.30 and 329.41 kg/m² s, respectively, and different water mass velocities.
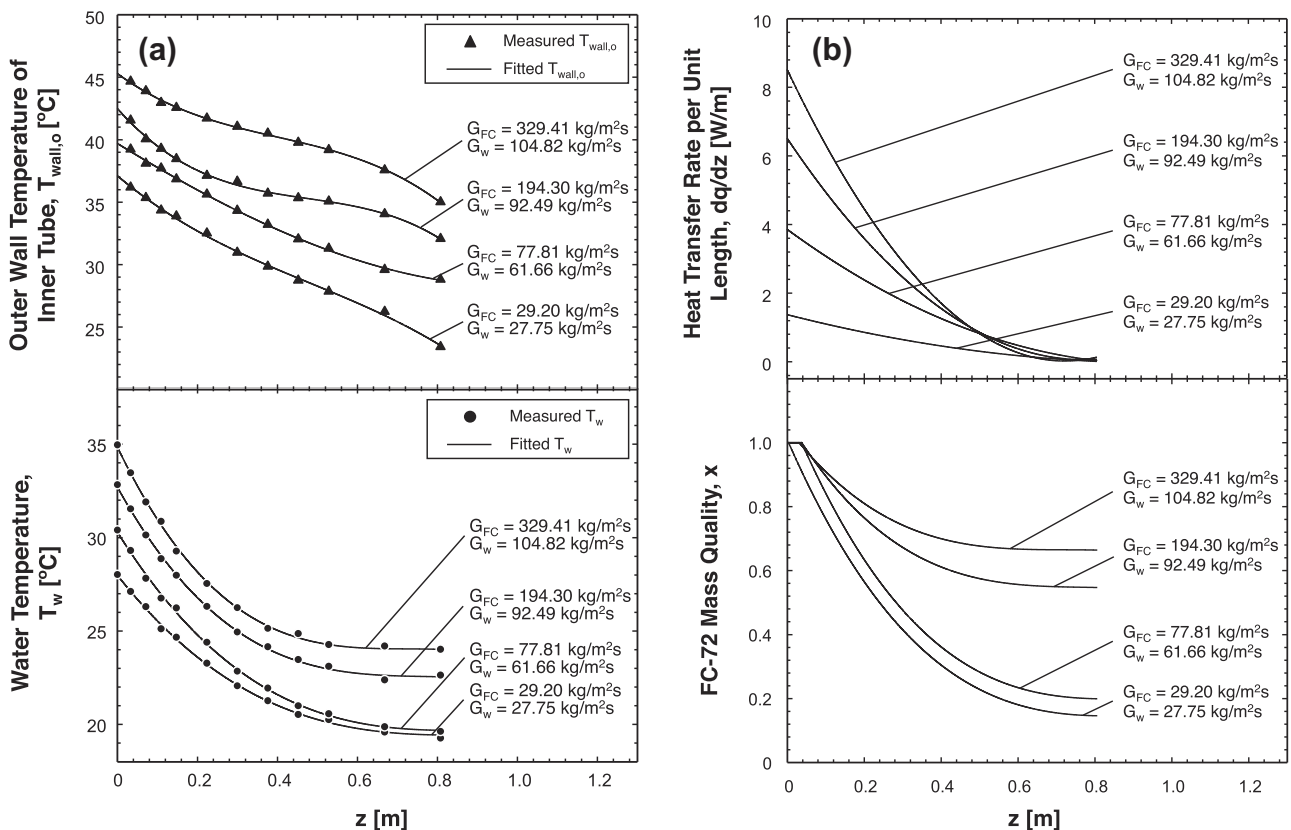

Fig. 9. Axial variations of (a) measured and fitted temperatures of outer wall of inner tube and cooling water, and (b) heat transferred from FC-72 to cooling water per unit distance and quality of FC-72 for different combinations of FC-72 and water mass velocities.

The heat transfer coefficient is relatively low in the superheated vapor region near the inlet for most cases, and increases rather sharply to peak value where the annular liquid film is initiated. Note that a clearly defined single-phase vapor flow region upstream of the peak point would yield a fairly constant h value. The unexpected trend of increasing h in the same upstream region may be explained by the film condensation commencing in a circumferentially nonuniform manner within the predominantly single-phase vapor region where $x_e > 1$. The peak value is believed to occur where nearly full coverage of the inner circumference by the liquid film is achieved. As shown in Fig. 10(a)–(d), h decreases along the condensation length downstream of the peak value for all FC-72 mass velocities. This trend is the result of the condensation liquid film being thinnest where the annular film is initiated and gradually increasing in thickness along the condensation length. It should also be noted that heat transfer in the upstream thin film region is laminar and dominated by conduction across the film. This trend is fairly monotonic for all cases corresponding to the three lowest FC-72 mass velocities, Fig. 10(a)–(c). However, Fig. 10(d) shows h for G_{FC} = 329.41 kg/m² s and two G_w values reaches a minimum before increasing again towards the outlet. The downstream increase can be explained by the film turning turbulent, with the heat transfer potentially enhanced by the intensified interfacial waviness. Comparing Fig. 10(a)–(d) shows h generally increases with increasing FC-72 mass velocity, which can be attributed to thinning of the film by the increasing vapor shear.

Fig. 11(a)–(d) show the variations of h with thermodynamic equilibrium quality, x_e. These plots exclude the region from the inlet to the peak point captured in Fig. 10(a)–(d). Fig. 11(a)–(c) corresponding to the three lowest FC-72 mass velocities show a monotonic decline in h with decreasing x_e, which is the result of the aforementioned axial increase in film thickness. However, h for the highest FC-72 mass velocity and two water mass velocities, Fig. 11(d), reaches a downstream minimum before increasing slightly because of downstream turbulence and interfacial waviness. Notice in Fig. 11(d) that the downstream minimum is absent for the lower values of G_w. This can be explained by the low G_w values reducing heat transfer rate between the two fluids, which prevents the liquid film from attaining sufficiently high flow rates downstream to achieve sufficient turbulence and downstream waviness.

Fig. 12(a) shows the axial span of the four flow regimes over the 807.7-mm measurement length for six FC-72 mass velocities of G_{FC} = 29.20, 38.94, 58.39, 77.82, 97.31, and 116.74 kg/m² s. For each value of G_{FC}, there is a relatively short upstream superheated region. For the lowest mass velocity of G_{FC} = 29.20 kg/m² s, *falling film* flow is encountered over the entire two-phase region. As G_{FC} is increased to 38.94 kg/m² s, *oscillating film* flow is encountered for a short distance immediately downstream of the superheated region, and *falling film* flow farther downstream. Notice how multiple flow regimes are encountered for G_{FC} = 58.39, 77.82, and 97.31 kg/m² s, but only *climbing film* flow is prevalent for G_{FC} = 116.74 kg/m² s.
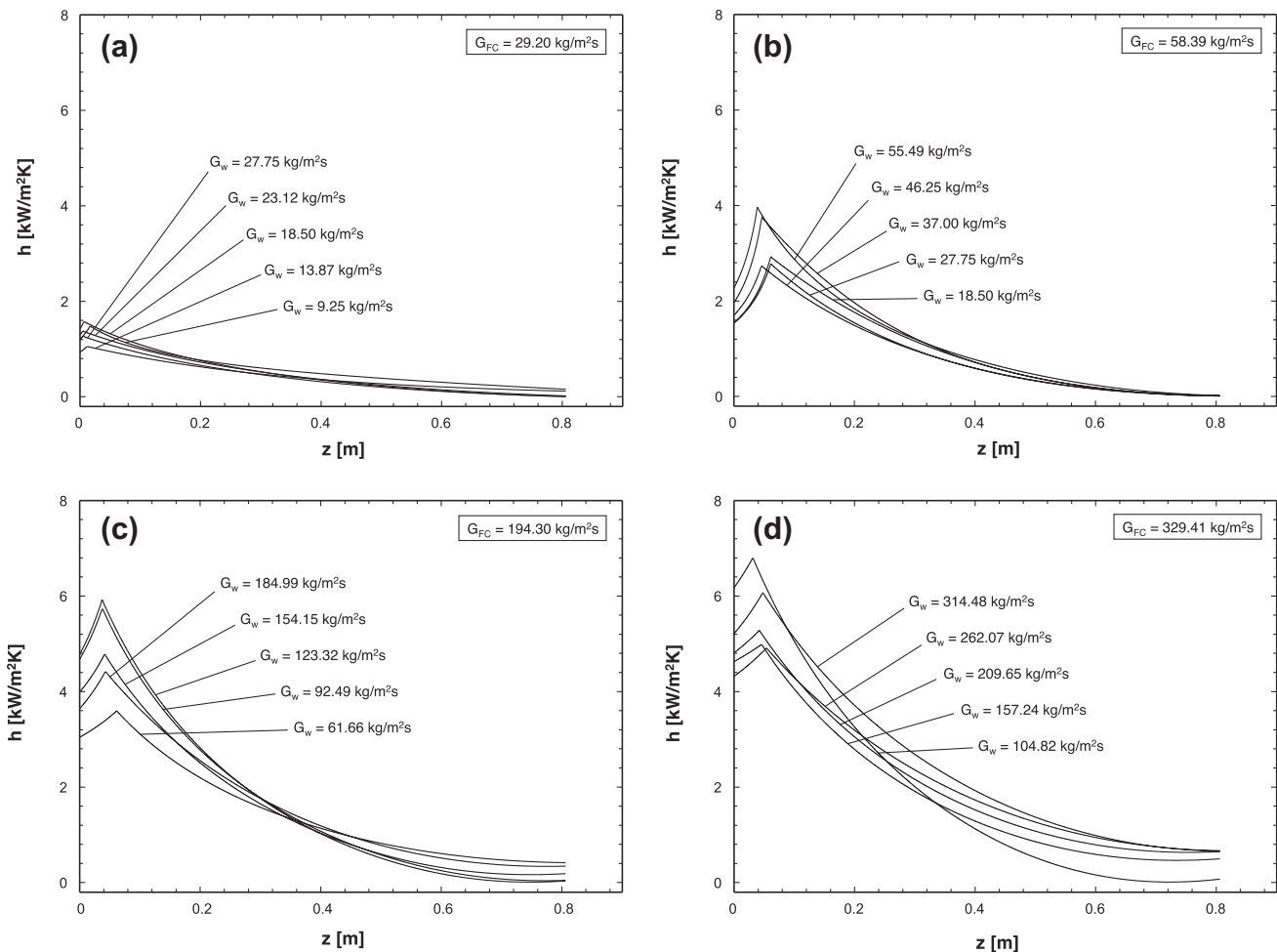

Fig. 10. Axial variation of experimentally determined local condensation heat transfer coefficient for different water mass velocities and FC-72 mass velocities of (a) G_{FC} = 29.20 kg/m² s, (b) G_{FC} = 58.39 kg/m² s, (c) G_{FC} = 194.30 kg/m² s, and (d) G_{FC} = 329.41 kg/m² s.
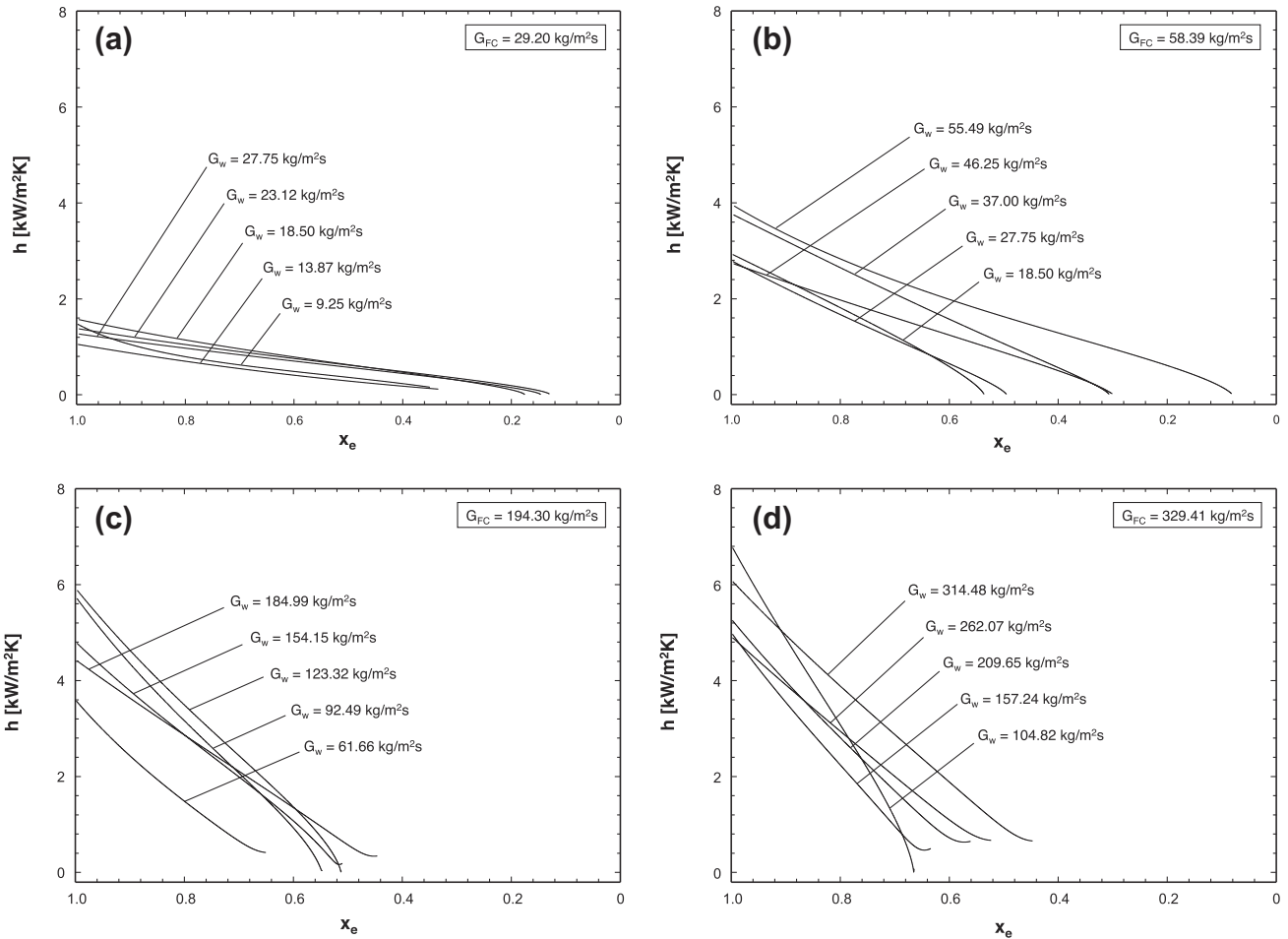
Fig. 11. Variation of experimentally determined local condensation heat transfer coefficient with thermodynamic equilibrium quality for different water mass velocities and FC-72 mass velocities of (a) G_{FC} = 29.20 kg/m² s, (b) G_{FC} = 58.39 kg/m² s, (c) G_{FC} = 194.30 kg/m² s, and (d) G_{FC} = 329.41 kg/m² s. These plots exclude the region captured in Fig. 13 from the inlet to the peak point.

Fig. 12(b) shows the variation of the average condensation heat transfer coefficient, $\bar{h}$, with exit film Reynolds number, $Re_{f,out}$. To determine $\bar{h}$, local heat transfer coefficient values are averaged over the 807.7-mm measurement length starting with the peak locations identified in Fig. 10(a)–(d), therefore excluding the upstream superheated vapor region. Notice that there is appreciable data scatter for $Re_{f,out}$ < 1600, where all four flow regimes are encountered. However, data for the *climbing film* regime show consistent and monotonic variation with $Re_{f,out}$.

5. Condensation model for climbing film regime

5.1. Limitations of annular flow model in upflow condensation

The results presented thus far prove that upflow condensation is quite complex, given the possibility of occurrence of multiple flow regimes along the condensation length as shown in Fig. 12(a). Of the four regimes discussed earlier, only *climbing film* flow may be effectively predicted using an annular flow model because of the concurrent flow of vapor and liquid.

However, the existence of the *climbing flow* regime is a necessary but not sufficient criterion for the applicability of an annular flow model. As shown in Fig. 12(a), *climbing film* flow occurs over the entire measurement length only for very high G_{FC}. This regime is nonexistent for the lowest G_{FC}, and occurs upstream of *flooding*, *oscillating film*, and/or *falling film* flows for intermediate values of

G_{FC}. For conditions where *climbing film* flow occurs upstream of other regimes, the applicability of the annular flow model may be compromised by downstream flow oscillations. Additionally, the annular flow solution procedure encounters a singularity when even a very small portion of the liquid in the climbing film flows downward.

Because of these limitations, the annular flow model is applicable only to conditions where (i) *climbing film* flow is encountered over a significant portion of the measurement length and (ii) all the liquid in the film flows concurrently upwards with the vapor. A simple criterion of climbing film flow occurring over 50% of the measurement length proved effective at satisfying both of these conditions. This limited the number of cases considered to 16 of the 69 operating conditions.

5.2. Formulation of annular flow model

Recently, Park et al. [53] developed a control volume model for annular flow corresponding to condensation in downflow. The model was based on the assumptions of smooth interface between the annular liquid film and vapor core, and circumferential symmetry of the liquid film. Since the present study concerns condensation in vertical upflow, the same model is adopted excepting the opposite orientation of gravity. This model is briefly summarized below with all the key equations provided in Table 4.
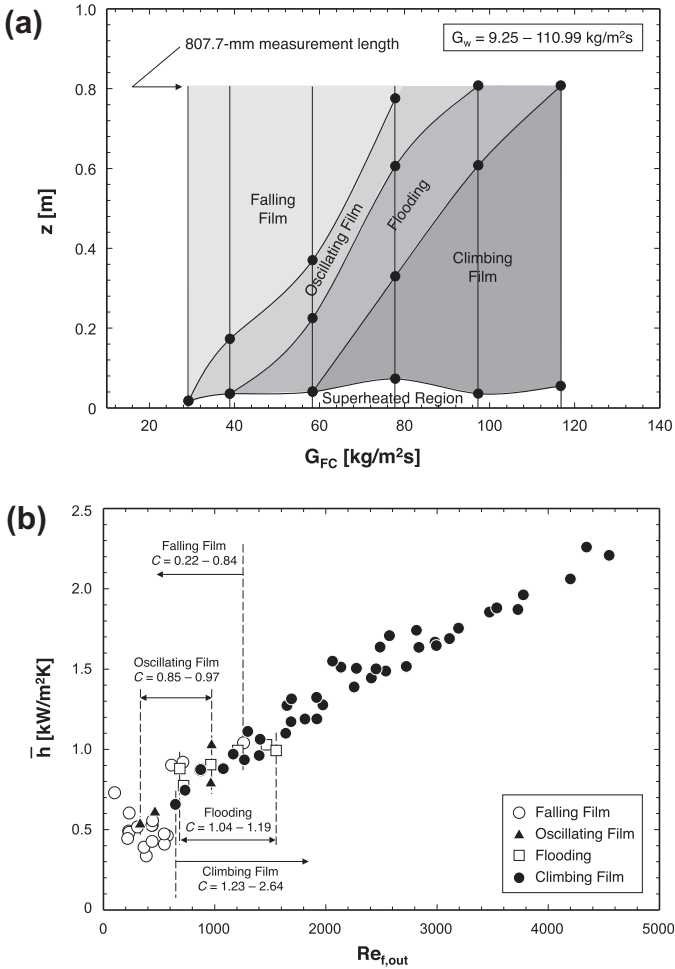
Fig. 12. (a) Variation of flow regimes along condensation length for different FC-72 mass velocities. (b) Variation of experimentally determined average FC-72 condensation heat transfer coefficient with film Reynolds number at the exit.

The annular flow model relies on the application of mass and momentum conservation to control volumes encompassing a portion of the liquid film and the entire vapor core as illustrated in Fig. 13(a). The mass flow rates of the liquid and vapor are given by $\dot{m}_f$ and $\dot{m}_g$, respectively, with Γ_{fg} representing the rate of interfacial mass transfer due to condensation per unit distance. First, mass conservation is applied to the differential liquid and vapor control volumes. Next, momentum conservation is applied to the liquid control volume, neglecting the film's axial momentum changes. This yields a relationship for the shear stress, τ, across the film, which is used to determine relations for liquid velocity, $u_f(y)$, and axial pressure gradient, $-dP/dz$. Momentum conservation is then applied to the vapor control volume, which yields a relation for the interfacial shear stress, τ_i, in terms of the pressure gradient. The relation for τ_i is equated to the definition of interfacial shear in terms of the product of interfacial friction factor, f_i, which is determined from relations by Shah and London [55], and velocity differences between the vapor core and interface. The interfacial shear stress is modified by the influence of interfacial momentum transfer due to condensation according to Wallis [30].

Heat flux across the liquid film is related to the liquid temperature gradient according to

$$\frac{q''}{q''_w} = \left(\frac{1}{\Pr_f} + \frac{1}{\Pr_T}\frac{\varepsilon_m}{\nu_f}\right)\frac{dT^+}{dy^+}, \tag{6}$$

where

Table 4
Annular flow model relations.

Mass conservation
$\frac{d\dot{m}_f}{dz} - \Gamma_{fg} = 0; \frac{d\dot{m}_g}{dz} + \Gamma_{fg} = 0 \dot{m}_f = \rho_f \int_0^\delta u_f \pi(D-2y)dy; \dot{m}_g$
$= \rho_g \bar{u}_g \pi(D-2\delta)^2/4; \Gamma_{fg} = q''_w \pi D/h_{fg}$

Momentum conservation for liquid film
$\tau = \mu_f\left(1 + \frac{\varepsilon_m}{\nu_f}\right)\frac{du_f}{dy} = \left(-\frac{dp}{dz} - \rho_f g\right)\frac{A_{f,*}}{P_{f,y}} + \frac{\tau_i P_{f,\delta} + \Gamma_{fg}u_i}{P_{f,y}}$
$A_{f,*} = \frac{\pi}{4}(D-2y)^2 - \frac{\pi}{4}(D-2\delta)^2, P_{f,y} = \pi(D-2y)P_{f,\delta} = \pi(D-2\delta)$

Velocity profile across the film
$u_f(y) = \frac{\delta}{\mu_f}\left(-\frac{dP}{dz} - \rho_f g\right)\int_0^{y/\delta}\frac{A_{f,*}}{P_{f,y}}\left(1 + \frac{\varepsilon_m}{\nu_f}\right)^{-1}d\left(\frac{y}{\delta}\right) + \frac{\delta}{\mu_f}(\tau_i P_{f,\delta} + \Gamma_{fg}u_i)$
$\int_0^{y/\delta}\frac{1}{P_{f,y}}(1 + \frac{\varepsilon_m}{\nu_f})^{-1}d\left(\frac{y}{\delta}\right); \quad u_i = u_f(\delta)$

Pressure gradient
$$-\frac{dP}{dz} = \rho_f g + \frac{\frac{\mu_f \dot{m}_f}{\rho_f \delta^2} - (\tau_i P_{f,\delta} + \Gamma_{fg}u_i)\int_0^1\left[P_{f,y}\int_0^{y/\delta}\frac{1}{P_{f,y}}\left(1 + \frac{\varepsilon_m}{\nu_f}\right)^{-1}d\left(\frac{y}{\delta}\right)\right]d\left(\frac{y}{\delta}\right)}{\int_0^1\left[P_{f,y}\int_0^{y/\delta}\frac{A_{f,*}}{P_{f,y}}\left(1 + \frac{\varepsilon_m}{\nu_f}\right)^{-1}d\left(\frac{y}{\delta}\right)\right]d\left(\frac{y}{\delta}\right)}$$

Momentum conservation for vapor core
$\tau_i = \frac{1}{P_{f,\delta}}\left[A_g\left(-\frac{dP}{dz} - \rho_g g\right) - \frac{d(\rho_g \bar{u}_g^2 A_g)}{dz} - \Gamma_{fg}u_i\right]; A_g = \pi(D-2\delta)^2/4$

Interfacial shear stress relation [30,55]
$\tau_i = \frac{1}{2}f_i \rho_g(\bar{u}_g - u_i)^2 + \frac{(\bar{u}_g - u_i)\Gamma_{fg}}{2P_{f,\delta}}$
$f_i = 16/\mathrm{Re}_c$ for $\mathrm{Re}_c < 2,000; f_i = 0.079\mathrm{Re}_c^{-0.25}$ for $2,000 \leqslant \mathrm{Re}_c < 20,000,$
$f_i = 0.046\mathrm{Re}_c^{-0.2}$ for $\mathrm{Re}_c \geqslant 20,000; \mathrm{Re}_c = \rho_g(\bar{u}_g - u_i)(D-2\delta)/\mu_g$

Eddy momentum diffusivity [55,58–60]
$\frac{\varepsilon_m}{\nu_f} = -\frac{1}{2} + \frac{1}{2}\sqrt{1 + 4K^2y^{+2}\left[1 - \exp\left(-\sqrt{1 - \frac{y^+}{\delta^+}}\frac{y^+}{A^+}\right)\right]^2\left(1 - \frac{y^+}{\delta^+}\right)\frac{\tau}{\tau_w}};$
$K = 0.4; A^+ = 26\left(1 + 30.18\mu_f \rho_f^{-0.5}\tau_w^{-1.5}\frac{dP}{dz}\right)^{-1}$

Turbulent Prandtl number [56]
$\Pr_T = 1.4\exp\left(-15\frac{y^+}{\delta^+}\right) + 0.66; \quad \delta^+ = \delta u^*/\nu_f$

Heat transfer coefficient
$h = \frac{q''_w}{T_{sat}-T_w} = \frac{\rho_f c_{p,f} u^*}{T_\delta^+} = \frac{\rho_f c_{p,f} u^*}{\int_0^{\delta^+}\frac{q''}{q''_w}\left(\frac{1}{\Pr_f} + \frac{1}{\Pr_T}\frac{\varepsilon_m}{\nu_f}\right)^{-1}dy^+} = \frac{\rho_f c_{p,f} u^*}{\int_0^{\delta^+}\left(\frac{D}{D-2\delta}\right)\left(\frac{1}{\Pr_f} + \frac{1}{\Pr_T}\frac{\varepsilon_m}{\nu_f}\right)^{-1}dy^+}$

$$T^+ = \frac{\rho_f c_{p,f} u^*(T - T_w)}{q''_w}, \tag{7}$$

$y^+ = yu^*/\nu_f$, $u^* = \sqrt{\tau_w/\rho_f}$, and $\Pr_T$ is the turbulent Prandtl number ($\varepsilon_m/\varepsilon_h$). The present model utilizes a relation for $\Pr_T$ that was derived by Mudawar and El-Masri [56] based on experimental data by Ueda et al. [57].

Based on Mudawar and El-Masri's turbulent mixing length profile [56], which incorporates an eddy-diffusivity profile measured by Ueda et al. [57], Kim and Mudawar [58] derived a relation for eddy momentum diffusivity in a shear-driven film that accounts for axial pressure gradient per [59,60]. This relation is used in the present model to determine the local condensation heat transfer coefficient by integrating Eq. (6)

$$h = \frac{q''_w}{T_{sat} - T_w} = \frac{\rho_f c_{p,f} u^*}{T_\delta^+} = \frac{\rho_f c_{p,f} u^*}{\int_0^{\delta^+}\frac{q''}{q''_w}\left(\frac{1}{\Pr_f} + \frac{1}{\Pr_T}\frac{\varepsilon_m}{\nu_f}\right)^{-1}dy^+}$$
$$= \frac{\rho_f c_{p,f} u^*}{\int_0^{\delta^+}\left(\frac{D}{D-2delta}\right)\left(\frac{1}{\Pr_f} + \frac{1}{\Pr_T}\frac{\varepsilon_m}{\nu_f}\right)^{-1}dy^+} \tag{8}$$

The model equations are solved numerically using a finite difference technique. The average heat transfer coefficient, $\bar{h}$, for the annular region is obtained by averaging $h(z)$ downstream of the peak values in Fig. 10(a)–(d).

5.3. Model predictions

Fig. 13(b) compares the model predictions of $\bar{h}$ with the experimental data. As indicated earlier, the experimental values examined here are for 16 cases with the *climbing film* occurring over 50% of the measurement length. The data are predicted with a

mean absolute error of 23.26%. One key reason for deviations between predicted and measured values is the influence of downstream flow oscillations and other flow regimes on the upstream *climbing film* flow. Another reason for the deviations is the inability of the annular model to account for the annular film's interfacial waviness. The importance of interfacial waves is evident from past
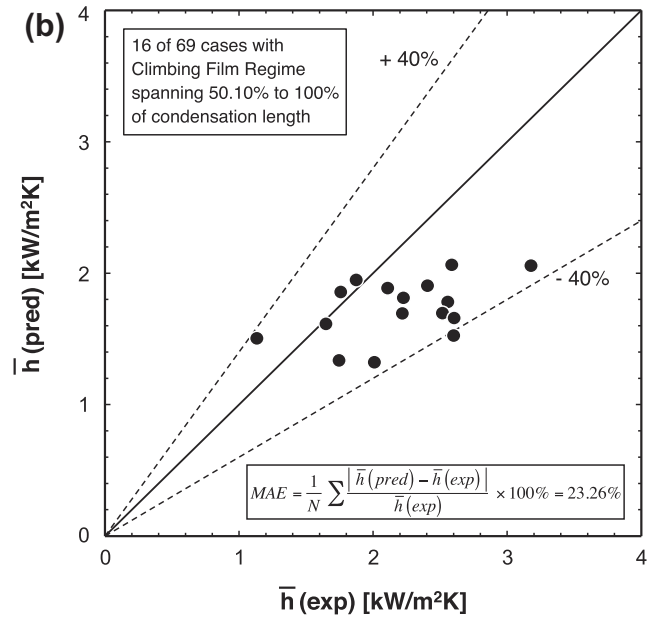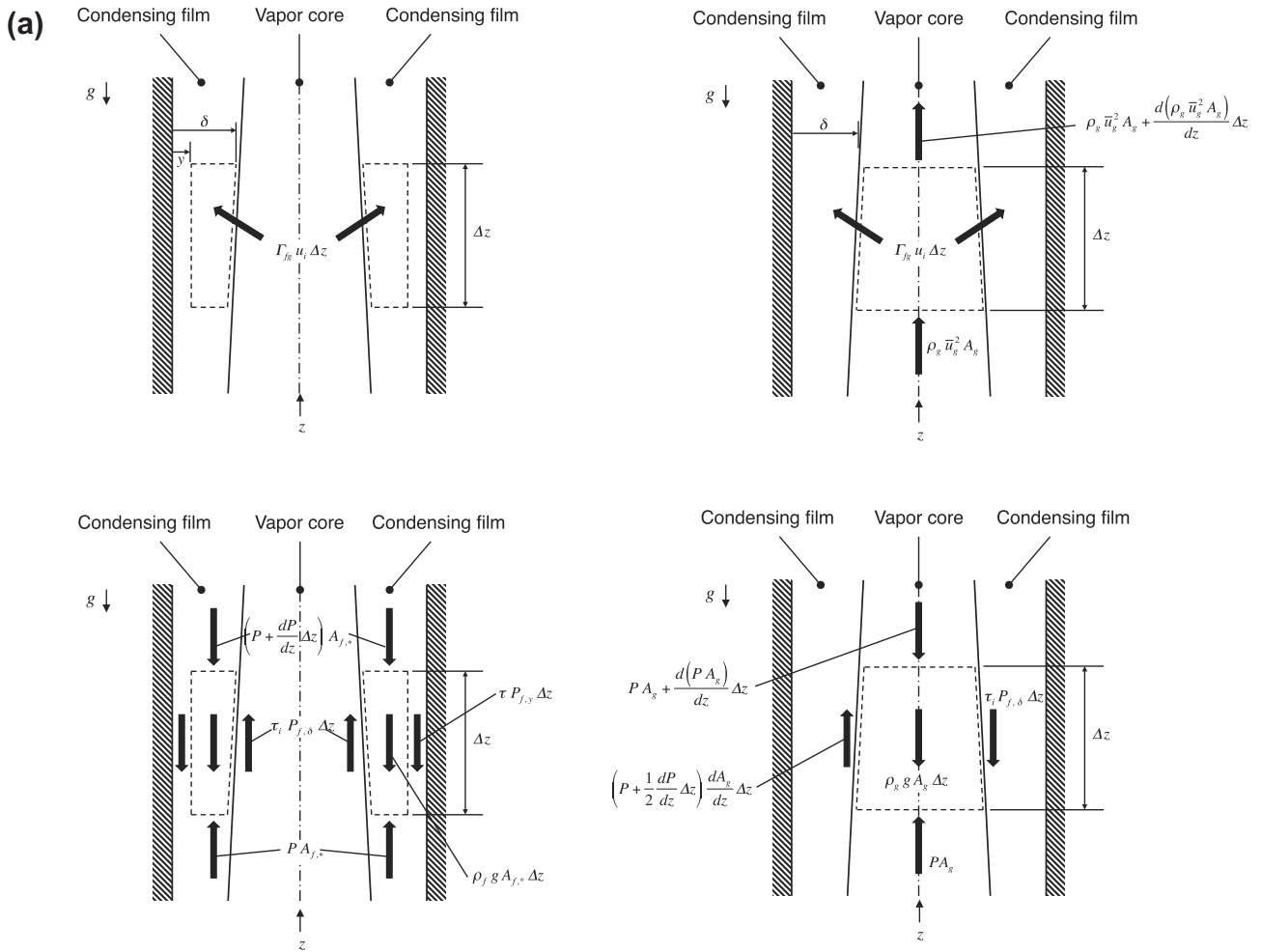

Fig. 13. (a) Momentum and force components for liquid film and vapor core control volumes. (b) Comparison of predicted and experimentally determined average condensation heat transfer coefficients for cases dominated by *climbing film* regime.

studies involving adiabatic, heated and evaporating liquid films [61–66]. Waviness can influence annular condensation in several ways, by increasing interfacial area, altering turbulence within the film, and causing fluctuations in film thickness with the wave peaks moving faster than the thinner substrate. It is therefore recommended that future models incorporate the influence of interfacial waviness in pursuit of superior predictions.

6. Conclusions

This study explored the various flow regimes encountered in upflow condensation of FC-72 in a vertical tube. Interfacial interactions were examined with the aid of high-speed video to segregate flow regimes and construct a comprehensive flow regime map. Heat transfer measurements were used to assess differences in heat transfer behavior between the different regimes. An annular flow model was constructed to predict heat transfer corresponding to concurrent upflow conditions. Key findings from the study are as follows.

(1) Four condensation regimes were identified, which, in the direction of increasing vapor velocity, are *falling film*, where the condensing film is driven downwards by gravity opposite to the vapor flow, *oscillating film*, where the film flow oscillates between upwards and downwards, *flooding*, where film begins to be carried upwards by the vapor shear, and *climbing film*, where the film motion is decidedly upwards as the vapor shear begins to dwarf the influence of gravity. The four flow regimes are well segregated in a map based on dimensionless superficial velocities of the vapor and liquid. Transition lines between the regimes are accurately predicted by the Wallis flooding relation [27] modified with different empirical coefficients.

(2) The local condensation heat transfer coefficient decreases along the condensation length because of gradual thickening of the film, except for high FC-72 mass velocities, where the heat transfer coefficient reaches a minimum before increasing downstream because of turbulence and intensified interfacial waviness. Overall, the heat transfer coefficient increases with increasing FC-72 mass velocity, which can be attributed to thinning of the film by the increasing vapor shear.

(3) The annular flow model is applicable only to the *climbing film* regime that features concurrent liquid and vapor flows. Deviations between predicted and measured values are attributed to the influence of downstream flow oscillations and inability of the model to account for interfacial waves.

Acknowledgment

Appendix A. Supplementary data

Supplementary data associated with this article can be found, in the online version, at http://dx.doi.org/10.1016/j. ijheatmasstransfer. 2013.05.065.

References

[1] I. Mudawar, Two-phase micro-channel heat sinks: theory, applications and limitations, J. Electron. Packag. Trans. ASME 133 (2011) 041002. 041002-2.

[2] T.M. Anderson, I. Mudawar, Microelectronic cooling by enhanced pool boiling of a dielectric fluorocarbon liquid, J. Heat Transfer Trans. ASME 111 (1989) 752–759.

[3] I. Mudawar, A.H. Howard, C.O. Gersey, An analytical model for near-saturated pool boiling CHF on vertical surfaces, Int. J. Heat Mass Transfer 40 (1997) 2327–2339.

[4] R.A. DeBortoli, S.J. Green, B.W. LeTourneau, M. Troy, A. Weiss, Forced-convection heat transfer burn-out studies for water in rectangular and round tubes at pressures above 500 psia, WAPD-188, Westinghouse Electric Corp., Pittsburgh, PA, 1958.

[5] T.C. Willingham, I. Mudawar, Forced-convection boiling and critical heat flux from a linear array of discrete heat sources, Int. J. Heat Mass Transfer 35 (1992) 2879–2890.

[6] M. Monde, T. Inoue, Critical heat flux in saturated forced convective boiling on a heated disk with multiple impinging jets, J. Heat Transfer Trans. ASME 113 (1991) 722–727.

[7] D.C. Wadsworth, I. Mudawar, Enhancement of single-phase heat transfer and critical heat flux from an ultra-high-flux-source to a rectangular impinging jet of dielectric liquid, J. Heat Transfer Trans. ASME 114 (1992) 764–768.

[8] M.E. Johns, I. Mudawar, An ultra-high power two-phase jet-impingement avionic clamshell module, J. Electron. Packag. Trans. ASME 118 (1996) 264–270.

[9] L. Lin, R. Ponnappan, Heat transfer characteristics of spray cooling in a closed loop, Int. J. Heat Mass Transfer 46 (2003) 3737–3746.

[10] M. Visaria, I. Mudawar, Theoretical and experimental study of the effects of spray orientation on two-phase spray cooling and critical heat flux, Int. J. Heat Mass Transfer 51 (2008) 2398–2410.

[11] R.L. Webb, The evolution of enhanced surface geometries for nucleate boiling, Heat Transfer Eng. 2 (1981) 46–69.

[12] V. Khanikar, I. Mudawar, T. Fisher, Effects of carbon nanotube coating on flow boiling in a micro-channel, Int. J. Heat Mass Transfer 52 (2009) 3805–3817.

[13] M.K. Sung, I. Mudawar, Experimental and numerical investigation of single-phase heat transfer using a hybrid jet-impingement/micro-channel cooling scheme, Int. J. Heat Mass Transfer 49 (2006) 682–694.

[14] M.K. Sung, I. Mudawar, Correlation of critical heat flux in hybrid jet impingement/micro-channel cooling scheme, Int. J. Heat Mass Transfer 49 (2006) 2663–2672.

[15] S.M. Kim, J. Kim, I. Mudawar, Flow condensation in parallel micro-channels – Part 1: Experimental results and assessment of pressure drop correlations, Int. J. Heat Mass Transfer 55 (2012) 971–983.

[16] H.M. Soliman, The mist-annular transition during condensation and its influence on the heat transfer mechanism, Int. J. Multiphase Flow 12 (1986) 277–288.

[17] H.M. Soliman, On the annular-to-wavy flow pattern transition during condensation inside horizontal tubes, Can. J. Chem. Eng. 60 (1982) 475–481.

[18] J.M. Mandhane, G.A. Gregory, K. Aziz, A flow pattern map for gas–liquid flow in horizontal pipes, Int. J. Multiphase Flow 1 (1974) 537–553.

[19] Q. Chen, R.S. Amano, M. Xin, Experimental study of flow patterns and regimes of condensation in horizontal three-dimensional micro-fin tubes, Int. J. Heat Mass Transfer 43 (2006) 201–206.

[20] S.M. Kim, I. Mudawar, Flow condensation in parallel micro-channels. Part 2: Heat transfer results and correlation technique, Int. J. Heat Mass Transfer 55 (2012) 984–994.

[21] G. Breber, J. Palen, J. Taborek, Prediction of horizontal tube-size condensation of pure components using flow regime criteria, J. Heat Transfer Trans. ASME 102 (1980) 471–476.

[22] C.O. Cersey, I. Mudawar, Effects of heater length and orientation on the trigger mechanism for near-saturated flow boiling critical heat flux – I. Photographic study and statistical characterization of the near-wall interfacial features, Int. J. Heat Mass Transfer 38 (1995) 629–641.

[23] C.O. Cersey, I. Mudawar, Effects of heater length and orientation on the trigger mechanism for near-saturated flow boiling critical heat flux – II. Critical heat flux model, Int. J. Heat Mass Transfer 38 (1995) 643–654.

[24] H. Zhang, I. Mudawar, M.M. Hasan, Experimental assessment of the effects of body force, surface tension force, and inertia on flow boiling CHF, Int. J. Heat Mass Transfer 45 (2002) 4079–4095.

[25] H. Zhang, I. Mudawar, M.M. Hasan, A method for assessing the importance of body force on flow boiling CHF, J. Heat Transfer Trans. ASME 126 (2004) 161–168.

[26] G. Bankoff, S.C. Lee, A critical review of the flooding literature, Multiphase Science and Technology, vol. 2, Hemisphere Publishing Corporation, New York, 1986.

[27] G.B. Wallis, Flooding velocities for air and water in vertical tubes, No. AEEW-R-123, United Kingdom Atomic Energy Authority, Reactor Group, Atomic Energy Establishment, Winfrith, Dorset, England, 1961.

[28] F. Feind, Falling liquid films with countercurrent air flow in vertical tubes, VDI-Forschungscheft 481 (1960) 5–35.

[29] R. Clift, C.L. Pritchard, R.M. Nedderman, The effect of viscosity on the flooding conditions in wetted wall columns, Chem. Eng. Sci. 21 (1966) 87–95.

[30] G.B. Wallis, One-dimensional Two-phase Flow, McGraw-Hill, New York, 1969.

[31] H. Imura, H. Kusuda, S. Funatsu, Flooding velocity in a counter-current annular two-phase flow, Chem. Eng. Sci. 32 (1977) 79–87.

[32] S. Suzuki, T. Ueda, Behaviour of liquid films and flooding in counter-current two-phase flow – Part 1. Flow in circular tubes, Int. J. Multiphase Flow 3 (1977) 517–532.

[33] A. Zapke, D.G. Kröger, The influence of fluid properties and inlet geometry on flooding in vertical and inclined tubes, Int. J. Multiphase Flow 22 (1996) 461–472.

[34] A. Zapke, D.G. Kröger, Countercurrent gas–liquid flow in inclined and vertical ducts – I: Flow patterns, pressure drop characteristics and flooding, Int. J. Multiphase Flow 26 (2000) 1439–1455.

[35] A. Zapke, D.G. Kröger, Countercurrent gas–liquid flow in inclined and vertical ducts – II: The validity of the Froude–Ohnesorge number correlation for flooding, Int. J. Multiphase Flow 26 (2000) 1457–1468.

[36] A.A. Mouza, S.V. Paras, A.J. Karabelas, The influence of small tube diameter on falling film and flooding phenomena, Int. J. Multiphase Flow 28 (2002) 1311–1331.

[37] A.A. Mouza, M.N. Pantzali, S.V. Paras, Falling film and flooding phenomena in small diameter vertical tubes: the influence of liquid properties, Chem. Eng. Sci. 60 (2005) 4981–4991.

[38] S. Fiedler, B. Thonon, H. Auracher, Flooding in small-scale passages, Exp. Therm. Fluid Sci. 26 (2002) 525–533.

[39] Y. Koizumi, T. Ueda, Initiation conditions of liquid ascent of the countercurrent two-phase flow in vertical pipes (in the presence of two-phase mixture in the lower portion), Int. J. Multiphase Flow 22 (1996) 31–43.

[40] K.S. Chung, C.P. Liu, C.L. Tien, Flooding in two-phase counter current flows – II: Experimental investigation, Physicochem. Hydrodyn. 1 (1980) 209–220.

[41] S. Fiedler, H. Auracher, Experimental and theoretical investigation of reflux condensation in an inclined small diameter tube, Int. J. Heat Mass Transfer 47 (2004) 4031–4043.

[42] U. Gross, Reflux condensation heat transfer inside a closed thermosyphon, Int. J. Heat Mass Transfer 35 (1992) 279–294.

[43] J.C.Y. Wang, Y. Ma, Condensation heat transfer inside vertical and inclined thermosyphons, J. Heat Transfer Trans. ASME 113 (1991) 777–780.

[44] C.J. Shearer, J.F. Davidson, The investigation of a standing wave due to gas blowing upwards over a liquid film; its relation to flooding in wetted-wall columns, J. Fluid Mech. 22 (1965) 321–335.

[45] A.G. Cetinbudaklar, G.J. Jameson, The mechanism of flooding in vertical countercurrent two-phase flow, Chem. Eng. Sci. 24 (1969) 1669–1680.

[46] C.L. Tien, K.S. Chung, C.P. Liu, Flooding in two-phase counter-current flows – I: Analytical modeling, Physicochem. Hydrodyn. 1 (1980) 195–207.

[47] P.B. Whalley, K.W. McQuillan, Flooding in two-phase flow: the effect of tube length and artificial wave injection, Physicochem. Hydrodyn. 6 (1985) 3–21.

[48] R. Girard, J.S. Chang, Reflux condensation phenomena in single vertical tubes, Int. J. Heat Mass Transfer 35 (1992) 2203–2218.

[49] Y. Taitel, D. Barnea, A.E. Dukler, A film model for the prediction of flooding and flow reversal for gas–liquid flow in vertical tubes, Int. J. Multiphase Flow 8 (1982) 1–10.

[50] M. Stephan, F. Mayinger, Experimental and analytical study of countercurrent flow limitation in vertical gas/liquid flows, Chem. Eng. Technol. 15 (1992) 51–62.

[51] C.E. Lacy, A.E. Dukler, Flooding in vertical tubes – II. A film model for entry region flooding, Int. J. Multiphase Flow 20 (1994) 235–247.

[52] S. Jayanti, A. Tokarz, G.F. Hewitt, Theoretical investigation of the diameter effect on flooding in countercurrent flow, Int. J. Multiphase Flow 22 (1996) 307–324.

[53] I. Park, S.M. Kim, I. Mudawar, Experimental measurement and modeling of downflow condensation in a circular tube, Int. J. Heat Mass Transfer 57 (2013) 567–581.

[54] H. Lee, I. Mudawar, M.M. Hasan, Experimental and theoretical investigation of annular flow condensation in microgravity, Int. J. Heat Mass Transfer 61 (2013) 293–309.

[55] R.K. Shah, A.L. London, Laminar Flow Forced Convection in Ducts: A Source Book for Compact Heat Exchanger Analytical Data, Academic Press, New York, 1978.

[56] I. Mudawar, M.A. El-Masri, Momentum and heat transfer across freely-falling turbulent liquid films, Int. J. Multiphase Flow 12 (1986) 771–790.

[57] H. Ueda, R. Moller, S. Komori, T. Mizushima, Eddy diffusivity near the free surface of open channel flow, Int. J. Heat Mass Transfer 20 (1977) 1127–1136.

[58] S.M. Kim, I. Mudawar, Theoretical model for annular flow condensation in rectangular micro-channels, Int. J. Heat Mass Transfer 55 (2012) 958–970.

[59] W.M. Kays, Heat-transfer to transpired turbulent boundary-layer, Int. J. Heat Mass Transfer 15 (1972) 1023–1044.

[60] W.M. Kays, M.E. Crawford, Convective Heat and Mass Transfer, second ed., McGraw-Hill, New York, 1980.

[61] J.A. Shmerler, I. Mudawar, Local heat transfer coefficient in wavy free-falling turbulent liquid films undergoing uniform sensible heating, Int. J. Heat Mass Transfer 31 (1988) 67–77.

[62] J.A. Shmerler, I. Mudawar, Local evaporative heat transfer coefficient in turbulent free-falling liquid films, Int. J. Heat Mass Transfer 31 (1988) 731–742.

[63] T.H. Lyu, I. Mudawar, Statistical investigation of the relationship between interfacial waviness and sensible heat transfer to a falling liquid film, Int. J. Heat Mass Transfer 34 (1991) 1451–1464.

[64] T.H. Lyu, I. Mudawar, Determination of wave-induced fluctuations of wall temperature and convective heat transfer coefficient in the heating of a turbulent falling liquid film, Int. J. Heat Mass Transfer 34 (1991) 2521–2534.

[65] I. Mudawar, R.A. Houpt, Mass and momentum transport in falling liquid films laminarized at relatively high Reynolds numbers, Int. J. Heat Mass Transfer 36 (1993) 3437–3448.

[66] I. Mudawar, R.A. Houpt, Measurement of mass and momentum transport in wavy-laminar falling liquid films, Int. J. Heat Mass Transfer 36 (1993) 4151–4162.